AFRL-OSR-VA-TR-2014-0500

Integrated Plasmon Optic Circuits for Nonometric Sources and Sensors

R. K Jain

Center for High Technology Materials University of New Mexico

22 October 2014
Final Report

AIR FORCE RESEARCH LABORATORY
AF OFFICE OF SCIENTIFIC RESEARCH (AFOSR)/NX
ARLINGTON, VIRGINIA 22203
AIR FORCE MATERIEL COMMAND

Report Documentation Page

Form Approved
OMB No. 0704-0188

1. REPORT DATE	2. REPORT TYPE	3. DATES COVERED
22 OCT 2014	**N/A**	**01 JUL 2006 - 30 JUN 2009**

4. TITLE AND SUBTITLE	5a. CONTRACT NUMBER
Integrated Plasmon--‐Optic Circuitsfor Nanometric Sources and Sensors	**FA9550-06-1-0446**
	5b. GRANT NUMBER **FA9550-06-1-0446**
	5c. PROGRAM ELEMENT NUMBER
6. AUTHOR(S) **R. K. Jain**	5d. PROJECT NUMBER
	5e. TASK NUMBER
	5f. WORK UNIT NUMBER
7. PERFORMING ORGANIZATION NAME(S) AND ADDRESS(ES) **Center for High Technology Materials University of New Mexico 1313 Goddard, SE Albuquerque, NM 87106**	8. PERFORMING ORGANIZATION REPORT NUMBER
9. SPONSORING/MONITORING AGENCY NAME(S) AND ADDRESS(ES) **Air Force Office of Scientific Research Suite 325, Room 3112 875 Randolph Street Arlington, VA 22203-1768**	10. SPONSOR/MONITOR'S ACRONYM(S)
	11. SPONSOR/MONITOR'S REPORT NUMBER(S) **AFRL-OSR-VA-TR-2014-0500**

12. DISTRIBUTION/AVAILABILITY STATEMENT
Approved for public release, distribution unlimited

13. SUPPLEMENTARY NOTES

14. ABSTRACT

Objective 1: o To use metal--‐insulator--‐metal (MIM) tunnel junctions (TJs) as surface plasmon polariton (SPP) generators and detectors that are integrable into efficient plasmonic circuits of sub--‐micron dimensions o To demonstrate many of the key building blocks that will facilitate the construction of micron--‐sized integrated plasmonic circuits Methodology (for Objective 1): o Design & demonstrate nanostructured MIM tunnel junctions as efficient SPP generators (SPGs) and light emitters with > 5% electrical--‐to--‐SPP power conversion efficiency and > 1% electrical--‐to--‐optical power conversion efficiency o Design & demonstrate low--‐loss (< 10 dB/mm) SPP waveguides (SPWs) that are compatible for excitation by TJs (see schematic figure below) o Demonstrate high (>10 %) coupling efficiencies from optimized tunnel junctions (TJs) into optimized SPWs o Build a simple plasmonic circuit with at least one internal Y--‐branch

15. SUBJECT TERMS

16. SECURITY CLASSIFICATION OF:			17. LIMITATION OF ABSTRACT	18. NUMBER OF PAGES	19a. NAME OF RESPONSIBLE PERSON
a. REPORT **unclassified**	b. ABSTRACT **unclassified**	c. THIS PAGE **unclassified**	**UU**	**36**	

Final Report

Performance Period: July 1, 2006 to June 30, 2009

AFOSR Contract #: FA9550-06-1-0446

Integrated Plasmon-Optic Circuits for Nanometric Sources and Sensors

PI: R. K. Jain

Center for High Technology Materials

University of New Mexico

1313 Goddard, SE

Albuquerque, NM 87106

1. **Cover Page (see above)**

2. **Objectives, Methodology, and Summary of Planned Technical Approach**:

- **Objective 1:**
  - To use metal-insulator-metal (MIM) tunnel junctions (TJs) as surface plasmon polariton (SPP) generators and detectors that are integrable into efficient plasmonic circuits of sub-micron dimensions
  - To demonstrate many of the key "building blocks" that will facilitate the construction of micron-sized integrated plasmonic circuits
- **Methodology (for Objective 1):**
  - Design & demonstrate nanostructured MIM tunnel junctions as efficient SPP generators (SPGs) and light emitters with > 5% electrical-to-SPP power conversion efficiency and > 1% electrical-to-optical power conversion efficiency
  - Design & demonstrate low-loss (< 10 dB/mm) SPP waveguides (SPWs) that are compatible for excitation by TJs (see schematic figure below)
  - Demonstrate high (>10 %) coupling efficiencies from optimized tunnel junctions (TJs) into optimized SPWs
  - Build a simple plasmonic circuit with at least one internal Y-branch

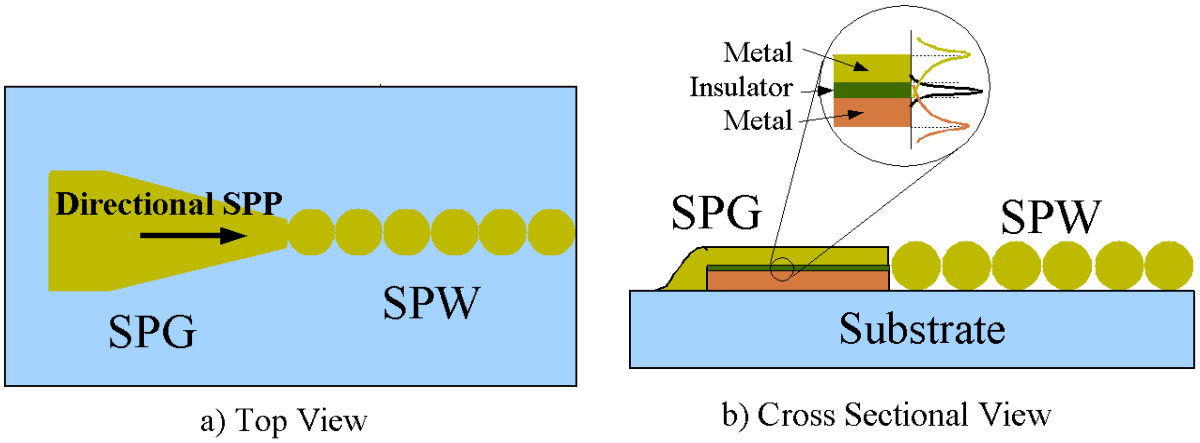

Figure 1: top view and cross sectional view of MIM tunnel junction

- **Technical Approach (Objective 1):**
  - Fabricate reliable and rugged TJs using thin films of metals M1 and M2 (M2 = Au or Ag) and a thin insulating barrier; optimize barrier material and width, evidenced by rugged tunnel junctions operable at voltages of over 3 Volts with large current densities and reproducible tunneling characteristics
  - Nanostructure one or both electrodes, initially randomly and subsequently with precise periodic nanoscale gratings (see figure below), and study the angular emission and spectral characteristics of light emission from TJs, particularly in the near-IR & mid-IR

- Use information learned in above-described experiments to create long-λ SPPs that propagate away from the TJ via transmission lines (TLs) to distances d ≥ 1 mm, and are observable via ***off-junction*** near-IR and mid-IR light emission (see figure below)
- Vary "d" while keeping all other parameters constant to measure the attenuation coefficient of the specific SPP modes excited.

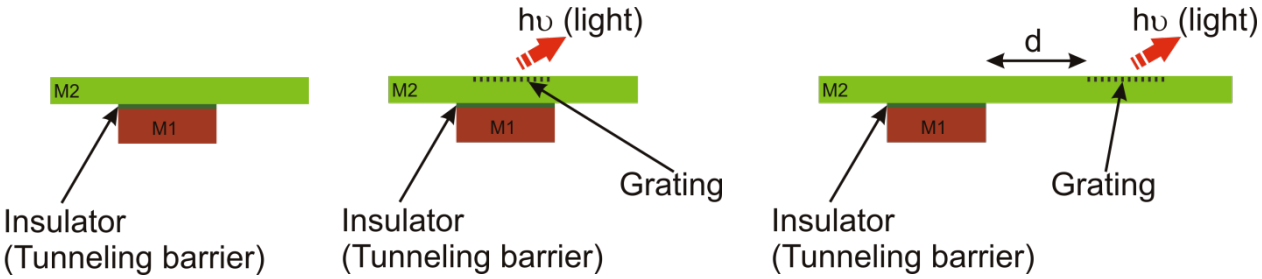

Figure 2: approaches to realize off-junction light emission by gratings

- **Objective 2:**
  - To study the nonlinear optical properties of semiconductor quantum dots, and to investigate interactions between semiconductor quantum dots and noble metal nanoparticles (and/or thin films)
  - To explore the utility of such interactions for novel applications, notably the use of semiconductor quantum dot and metallic nanoparticle coupled structures for SPW "spaser-like" amplifiers and nonlinear optical imaging

- **Technical Approach (Objective 2):**
  - Fabricate monolayers of semiconductor quantum dots (QDs) and metal thin film/nanocrystals that are separated by precisely-controlled nanometer "spacer" SiO_2 layers (see figure below)

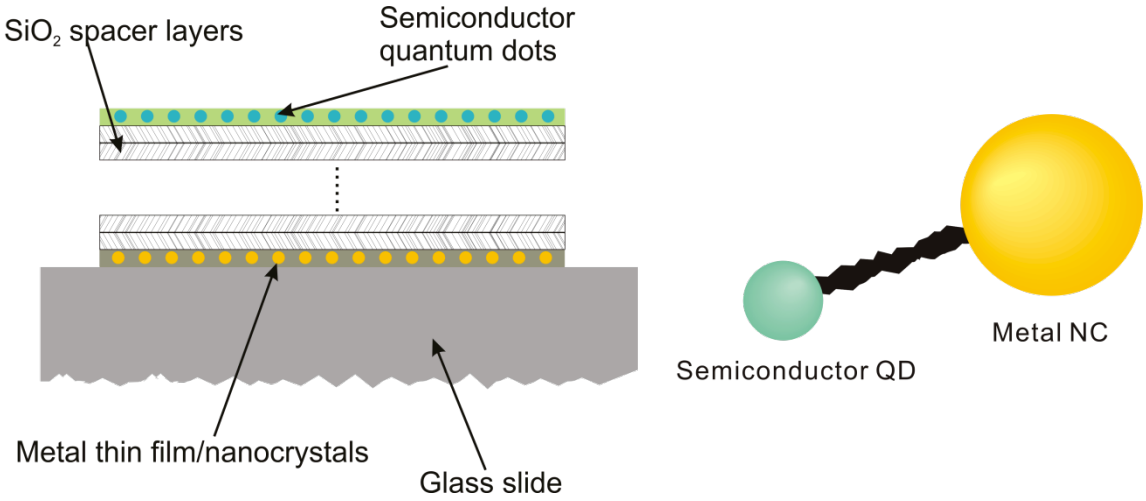

Figure 3: (a) schematic of the ayer by layer structures, (b) schematic drawing of the composite "molecule" for enhanced fluorescence in bio-imaging applications

  - Study plasmon-mediated linear and nonlinear (TPA) fluorescence from QDs as a function of the thickness of the spacer layer (varied from < 5 nm to > 25 nm)
  - Fabricate metal-semiconductor composite structures, and repeat above studies with a focus on geometries leading to SPP amplification and enhanced-sensitivity two-photon imaging applications

3. Accomplishments/New Findings:

a. Fabricated Al-Al_2O_3-Ag and Al-Al_2O_3-Au TJs and studied I-V characteristics
b. Masks were designed and fabricated, incorporating transmission lines (10 mm < d < 100 mm) and nanostructured gratings (period ~ 90 nm)
c. Fabrication of high reliability junctions that were rugged and reproducible was a problem, and limited our ability to conduct reliable SPP transmission and coupling (via light emission) experiments.
d. Designed advanced nanostructures that can be fabricated very efficiently with a DPN lithography system
e. Used 4 nm CdSe/ZnS quantum dots and 20 nm thick Au films, excited by 410 nm and 820 nm radiation for linear and nonlinear (TPA) fluorescence studies respectively
f. Linear fluorescence was enhanced at a spacer thickness of 15 nm, indicating that the SP-induced "local field enhancement" dominates over electron tunneling-induced quenching at these distances
g. Nonlinear TPA-induced fluorescence was always quenched for the range of spacings (0 to 15 nm) studied, presumably because the excitation wavelength was far from the Au plasmon frequency, implying a very weak interaction of the QD fluorophores with the SPs.

- **Objective 1 Accomplishments:**
  - Fabricated Al-Al_2O_3-Au TJs and studied I-V characteristics: IV curves of Al-Al_2O_3-Au (Al thickness: 90 nm, Al_2O_3 thickness: 3.5 nm, Au thickness: 25 nm, junction area: 2 mm x 2 mm) junctions showed excellent tunneling characteristics

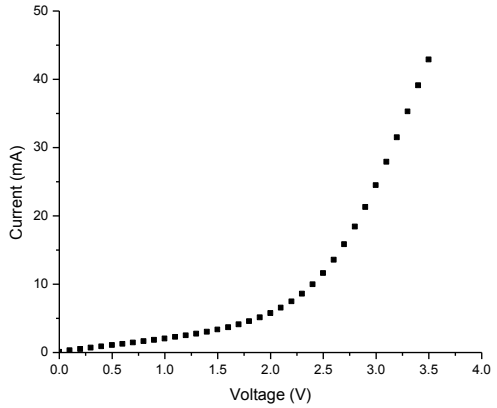

Figure 4. I-V curves for Al-Al_2O_3-Au TJs

  - Have measured the emission spectrum of such junctions with and without random roughness. The random roughness was created by depositing 10 nm diameter Au nanoparticles on top of the junction and also by inserting a 150 nm of MgF2 sublayers between substrate and bottom electrode of the junction.

- Au nanoparticles (10 nm diameter) were deposited on the junction by drop casting of Au nanoparticle solution (with a concentration of $5.7x10^{12}$/mL in water) on the junction and drying naturally.
- MgF_2 (thickness of 150 nm) were deposited on the glass substrate by dielectric evaporator, which has an rms roughness of 20 nm statistically. Such roughness was transferred to the top of the junction if very thin layer of Au and Al films were deposited.
- We have observed a blue shift of the spectrum of the junctions with Au NPs. The emission intensity drop was presumably caused by water infiltration into the oxide layer and increasing the thickness of oxide, which was also verified by the drop of current at the same time.
- Junctions with MgF_2 layer have much stronger emission than those without, as shown in figure below.

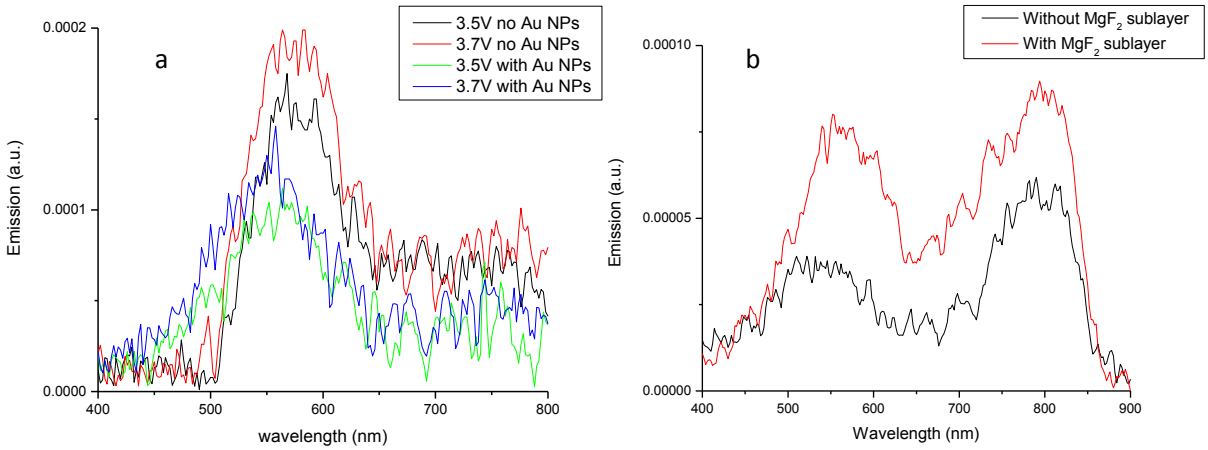

Figure 5: emission spectrum from junctions with random roughness, which were created by: (a) Au nanoparticles and (b) MgF_2 layer

- Longer wavelength plasmons were generated with high bias, see figure 6 below; We attributed this long wavelength emission to the change of junction surface, see Figure 7
- When bias was increased from 4.0 V to 4.1 V, a much stronger peak (centered at ~ 800 nm with full width at half maximum of ~ 120 nm) was observed.

- Besides above randomly roughed tunnel junction, highly periodic structures have also been tried, collaborating with Dr. Brinker in Sandia labs. A monolayer of well structured Au nanoparticle (5.6 nm in diameter) was put on the top of the junction. (The fabrication details of the Au NP thin film were similar to those of Pang et al, "Free-Standing, Patternable Nanoparticle/Polymer Monolayer Arrays Formed by Evaporation Induced Self-Assembly at a Fluid Interface", JACS Comm., **130**, p3284 (2008)). Efficient luminescent emission was observed with such well -patterned films.

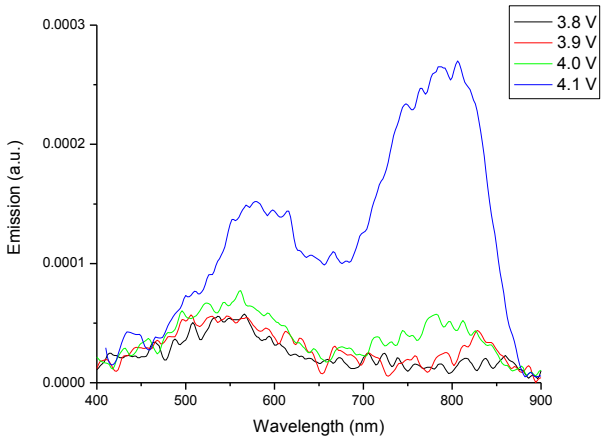

Figure 6: Longer wavelength emission from tunnel junctions with higher bias

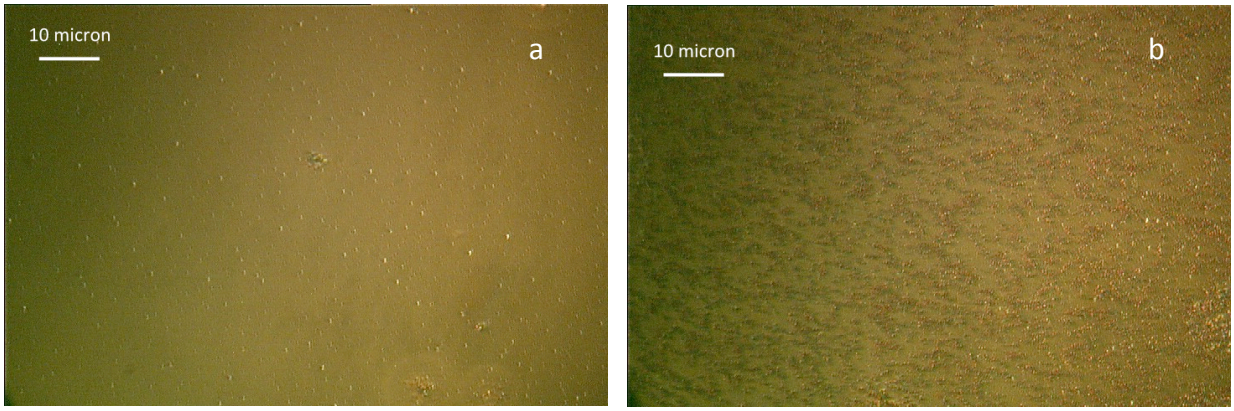

Figure 7: Images of junction surface (a) before and (b) after spectral measurement

- Longer wavelength plasmons have much smaller propagation losses. Such a demonstration shows the possibility of using longer wavelength plasmons in the design of the transmission line and makes future integrated SPP circuits – based on on-chip electrical excitation much more realistic.

- Masks were designed and fabricated, incorporating transmission lines (10 mm < d < 100 mm) and nanostructured gratings (period ~ 90 nm)
- Designed advanced nanostructures that can be fabricated very efficiently with a DPN lithography system

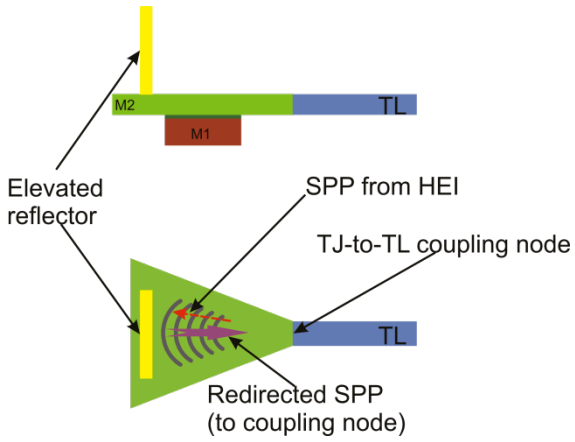

Figure 8: schematic drawing of the elevated reflector design for efficient collection of SPs.

- **Findings and Future Recommendations (Objective 1):**
  - Fabricate more rugged and reliable TJs by using combinations of *in situ* native oxide growth and sputter deposition of insulating barriers
  - Model and develop improved device designs that:
    - incorporate advanced techniques for re-direction (focusing) of SPP energy to the node between TJ and TL,
    - optimize SPP coupling from TJ structure to TL structure,
    - use long-λ fast mode SPP's to ensure low-loss SPP propagation on TL, and
    - achieve high-efficiency coupling of SPP's from TL to light (via optimization of nanostructured gratings)
    - fabricate such structures with a dip-pen lithography (DPN) system

- **Objective 2 Accomplishments**:

  - Fabrication of high quality Au NP thin films
    - Commercially available Au NPs are usually available in aqueous colloidal solutions, which are harder to use to form a high quality gold thin film via conventional methods, like spin coating
    - We developed a procedure to fabricate high quality Au NP thin films with a much easier process and less contamination from other chemicals.
    - Scanning electron microscope images of such films are shown in Figure 9 below.

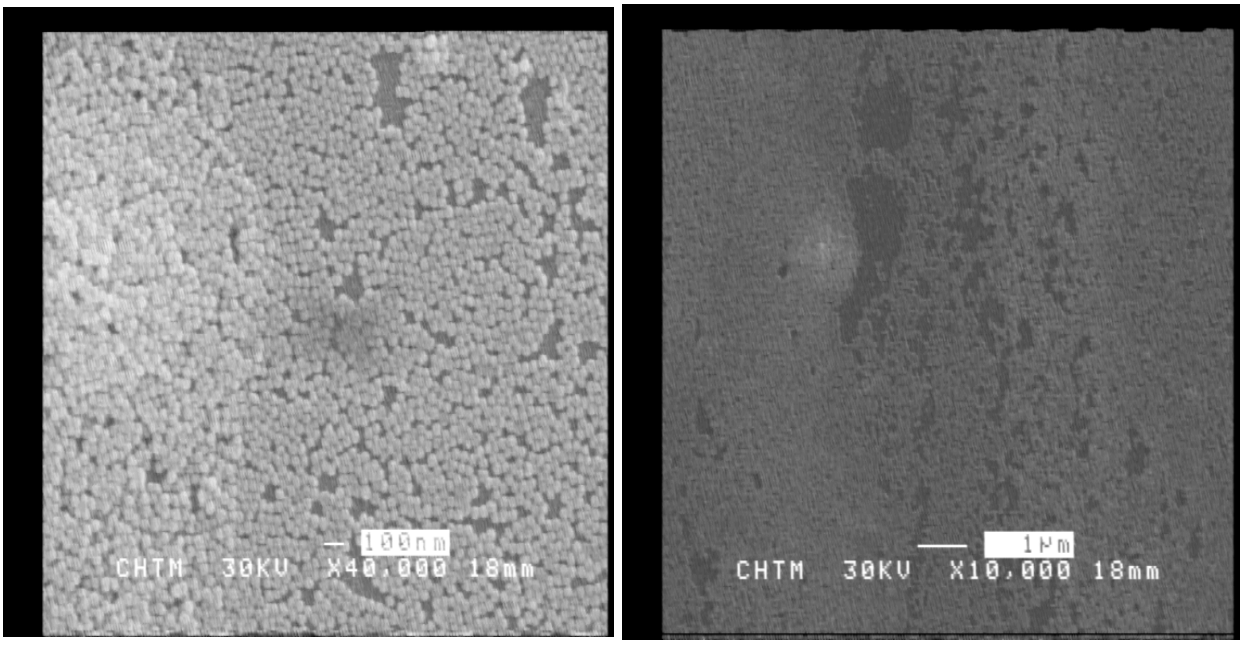

Figure 9: SEM images of 50 nm diameter Au NP thin films that were deposited on glass slide

- Used 4 nm CdSe/ZnS quantum dots and such fabricated Au NP films, excited by 400 nm radiation for linear fluorescence study. And the spacer layer is about 15 nm. Linear fluorescence was enhanced, indicating that the QDs radiate more efficiently because the SP-induced "local field enhancement" dominates over electron tunneling-induced quenching at these distances (see Figure 10 below).

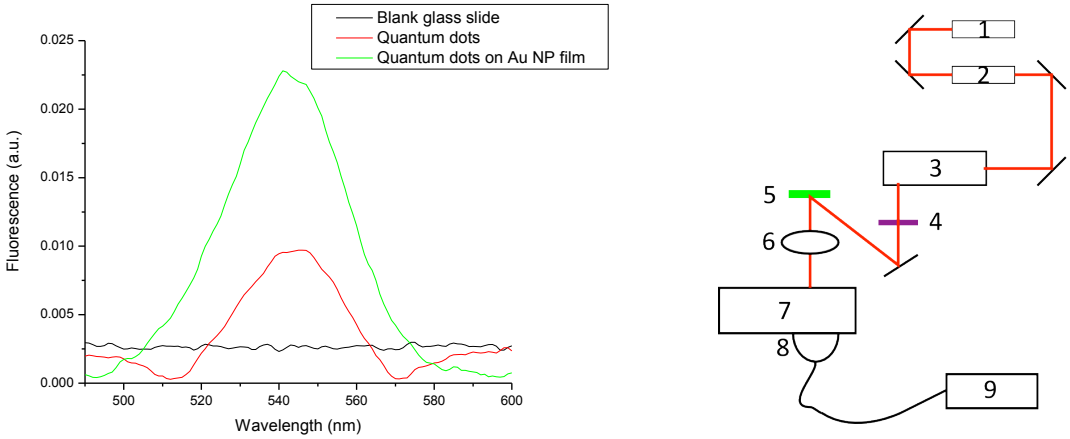

Figure 10: (a) linear fluorescence enhancement of semiconductor quantum dots by 50 nm Au NPs, (b) Schematic of the fluorescence lifetime measurement setup: 1: 20 W argon laser, 2: mode-locked Ti:sapphire laser, 3: second-harmonic generation, 4: acoustic optical modulator, 5: sample, 6: focusing lens, 7: ½-meter monochromator, 8: photon multiplier

- Fluorescence lifetimes were measured on QD samples with and without the Au NPs. A schematic of the setup is shown in figure 8. Preliminary results showed a lifetime increase of over 10 ns of the fluorescence from QDs on Au NPs.
- Used 4 nm CdSe/ZnS quantum dots and 20 nm thick Au films, excited by 820 nm radiation for the nonlinear (TPA) fluorescence study. Nonlinear TPA-induced fluorescence was always quenched for the range of spacings (0 to 15 nm) studied, presumably because the excitation wavelength is far from the Au plasmon frequency, implying a very weak interaction of the QD fluorophores with the SPs, see Figure 11.

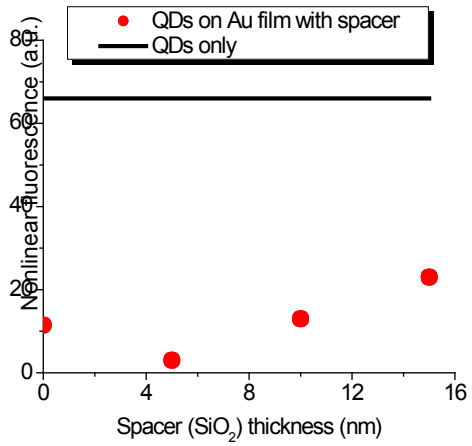

Figure 11: Quenching of nonlinear fluorescence by 20 nm thick Au thin film

Relevance and Potential Applications of Research to AF & Civilian Technology Needs:

- ***Objective 1***: This research may result in the first practical demonstration of an on-chip all-electronic SPP generator. Such a device would potentially change the field of plasmonics radically, enabling integrated plasmonic circuits, such that the entire sensor or info processing circuit may have overall dimensions of < 1 micron (enabling fabrication of a complete sensor system -- consisting of multivariate arrays -- in sub-mm sized packages)
- ***Objective 2***: A clear understanding of coupled interactions between metal nanoparticles and semiconductor quantum dots will enable the design and fabrication of optimized composite structures for "spaser"- type SPP amplifiers and high-sensitivity nonlinear imaging applications

5. **Personnel**:

   Faculty: R. K. Jain

   Students: Melissa Aillaud, Jiayu Chen, Damian Ankuciwiecz, William Zortman, Li Wang

6. **Publications**:

   a. L. Wang, D. Ankuciwiez, J. Chen, and R. K. Jain, "Surface-Plasmon Enhanced Fluorescence in CdSe/ZnS Semiconductor Quantum Dots," in Proceedings of Conference on Lasers and Electro-Optics/International Quantum Electronics Conference, 2009, Paper CTuO7; ***see Appendix B below.***

   b. L. Wang, D. Ankuciwiez, J. Chen, and R. K. Jain, "Enhancement of Two-Photon Absorption-Induced Florescence in Semiconductor Quantum Dots by Gold Nanoparticles," in Proceedings of Nonlinear Optics: Materials, Fundamentals and Applications, Optical Society of America, 2009, Paper NME4.

   c. L. Wang and R. K. Jain, "Optimization of TPA-Induced Fluorescence from Ultrasmall (< 2 nm) Semiconductor Quantum Dots Used for Deep Tissue Imaging," in Proceedings of Nonlinear Optics: Materials, Fundamentals and Applications, Optical Society of America, 2009, Paper NFB3.

   d. L. Wang and R. K. Jain, "Maximization of nonlinear fluorescence from ultrasmall (< 2 nm) semiconductor quantum dots to be used for deep tissue imaging," J. Opt. Soc. Am. B **26**, 2161-2166 (2009); ***see Appendix A below***.

   e. J. Y. Chen, D. Ancukiewicz, L. Wang, and R. K. Jain, "Near-IR Emission from Metal-Insulator-Metal Tunnel Junctions Based on Surface Plasmon Interactions," in Conference on Lasers and Electro-Optics (CLEO), Paper JTuD90; ***see Appendix F below***.

   f. J. Y. Chen, D. Ancukiewicz, L. Wang, and R. K. Jain, "Surface Plasmon Assisted Broadband Emission from Nanostructured Metal-Insulator-Metal Tunnel Junctions," in Integrated Photonics and Nanophotonics Research and Applications (IPNRA), Optical Soc. of America, 2009, Paper IME5; ***see Appendix C below.***

7. **Interactions/Translations**: None to date

8. **New Discoveries, Inventions, or Patent Disclosures**: None

9. **Honors/Awards**: Lifetime Achievement Honors (R.K. Jain): Fellow, OSA; Fellow, SPIE; Fellow, IEEE-LEOS; Harold Edgerton Award, SPIE.

10. **Appendices:** The following Appendices are preprints/reprints of a representative set of publications cited in Section 6 above.

Appendix A : Maximization of nonlinear fluorescence from ultrasmall (≤ 2 nm) semiconductor quantum dots to be used for deep tissue imaging

L. Wang and R. K. Jain*

Center for High Technology Materials, University of New Mexico,
1313 Goddard St SE, Albuquerque, NM 87106, USA
**Corresponding author: jain@chtm.unm.edu*

Abstract: We propose the use of ultrasmall semiconductor quantum dots (USQDs) for specialized bio-imaging applications, and discuss methods for enhancing fluorescent signals from USQDs to be used for two-photon absorption based deep tissue imaging. In particular, we report optimizing the excitation wavelength for two-photon absorption-induced fluorescence (TPAF) in CdSe/ZnS SQDs and demonstrate a 68-fold enhancement in the fluorescence signal when the TPAF excitation wavelength is changed from 900 nm to 780 nm.

OCIS codes: (170.3880) Medical and biological imaging; (190.0190) Nonlinear optics

References and links

1. W. Denk, J. H. Strickler, and W. W. Webb, "Two-photon laser scanning fluorescence microscopy," Science **248**, 73-76 (1990).
2. B. R. Masters, P. T. C. So, and E. Gratton, "Optical biopsy of in vivo human skin: Multi-photon excitation microscopy," Lasers Med. Sci. **13**, 196-203 (1998).
3. R. M. Williams, W. R. Zipfel, and W. W. Webb, "Multiphoton microscopy in biological research," Curr. Opin. Chem. Biol. **5**, 603-608 (2001).
4. D. R. Larson, W. R. Zipfel, R. M. Williams, S. W. Clark, M. P. Bruchez, F. W. Wise, and W. W. Webb, "Water-soluble quantum dots for multiphoton fluorescence imaging in vivo," Science **300**, 1434-1436 (2003).
5. J. M. Squirrell, D. L. Wokosin, J. G. White, and B. D. Bavister, "Long-term two-photon fluorescence imaging of mammalian embryos without compromising viability," Nat. Biotechnol. **17**, 763-767 (1999).
6. E. B. Brown, R. B. Campbell, Y. Tsuzuki, L. Xu, P. Carmeliet, D. Fukumura, and R. K. Jain, "In vivo measurement of gene expression, angiogenesis and physiological function in tumors using multiphoton laser scanning microscopy," Nat. Med. **7**, 864-868 (2001).
7. K. Svoboda, W. Denk, D. Kleinfeld, and D. W. Tank, "In vivo dendritic calcium dynamics in neocortical pyramidal neurons," Nature **385**, 161-165 (1997).
8. B. E. Chen, B. Lendvai, E. A. Nimchinsky, B. Burbach, K. Fox, and K. Svoboda, "Imaging high-resolution structure of GFP-expressing neurons in neocortex in vivo," Learn. Memory **7**, 433-441 (2000).
9. K. W. Dunn, R. M. Sandoval, K. J. Kelly, P. C. Dagher, G. A. Tanner, S. J. Atkinson, R. L. Bacallao, and B. A. Molitoris, "Functional studies of the kidney of living animals using multicolor two-photon microscopy," Am. J. Physiol.: Cell Physiol. **283**, C905-916 (2002).
10. V. E. Centonze, and J. G. White, "Multiphoton excitation provides optical sections from deeper within scattering specimens than confocal imaging," Biophys. J. **75**, 2015-2024 (1998).
11. X. Deng, and M. Gu, "Penetration depth of single-, two-, and three-photon fluorescence microscopic imaging through human cortex structures: Monte Carlo simulation," Appl. Opt. **42**, 3321-3329 (2003).
12. L. Sacconi, R. P. O'Connor, A. Jasaitis, A. Masi, M. Buffelli, and F. S. Pavone, "In vivo multiphoton nanosurgery on cortical neurons," J. Biomed. Opt. **12**, 050502 (2007).
13. M. Bruchez, Jr., M. Moronne, P. Gin, S. Weiss, and A. P. Alivisatos, "Semiconductor nanocrystals as fluorescent biological labels," Science **281**, 2013-2016 (1998).
14. W. C. W. Chan, and S. Nie, "Quantum dot bioconjugates for ultrasensitive nonisotopic detection," Science **281**, 2016-2018 (1998).
15. M. J. O'Donovan, S. Ho, G. Sholomenko, and W. Yee, "Real-time imaging of neurons retrogradely and anterogradely labelled with calcium-sensitive dyes," J. Neurosci. Methods **46**, 91-106 (1993).
16. M. Danek, K. F. Jensen, C. B. Murray, and M. G. Bawendi, "Synthesis of luminescent thin-film CdSe/ZnSe quantum dot composites using CdSe quantum dots passivated with an overlayer of ZnSe," Chem. Mater. **8**, 173-180 (1996).
17. C. B. Murray, D. J. Norris, and M. G. Bawendi, "Synthesis and characterization of nearly monodisperse CdE (E = S, Se, Te) semiconductor nanocrystallites," J. Am. Chem. Soc. **115**, 8706-8715 (1993).
18. P. T. Tran, E. R. Goldman, G. P. Anderson, J. M. Mauro, and H. Matroussi, "Use of luminescent CdSe-ZnS nanocrystal bioconjugates in quantum dot-based nanosensors," (Wiley-VCH, Germany, 2002), pp. 427-432.
19. D. Gerion, F. Pinaud, S. C. Williams, W. J. Parak, D. Zanchet, S. Weiss, and A. P. Alivisatos, "Synthesis and properties of biocompatible water-soluble silica-coated CdSe/ZnS semiconductor quantum dots," J. Phys. Chem. B **105**, 8861-8871 (2001).
20. W. J. Parak, D. Gerion, D. Zanchet, A. S. Woerz, T. Pellegrino, C. Micheel, S. C. Williams, M. Seitz, R. E. Bruehl, Z. Bryant, C. Bustamante, C. R. Bertozzi, and A. P. Alivisatos, "Conjugation of DNA to silanized colloidal semiconductor nanocrystalline quantum dots," Chem. Mater. **14**, 2113-2119 (2002).

21. S. Wang, N. Mamedova, N. A. Kotov, W. Chen, and J. Studer, "Antigen/Antibody immunocomplex from CdTe nanoparticle bioconjugates," Nano Lett. **2**, 817-822 (2002).
22. W. Guo, J. J. Li, Y. A. Wang, and X. Peng, "Conjugation chemistry and bioapplications of semiconductor box nanocrystals prepared via dendrimer bridging," Chem. Mater. **15**, 3125-3133 (2003).
23. L. Wang, Z. Zhang, R. K. Jain, F. Vanholsbeeck, S. Murdoch, and J. Harvey, "Measurement of two-photon absorption coefficients in colloidal semiconductor quantum dots," in *Proceedings of IEEE Lasers and Electro-Optics Society Annual Meeting*, Vol. # 2, (Institute of Electrical and Electronics Engineers Inc., New York, NY, 2004), pp. 487-488.
24. S.-C. Pu, M.-J. Yang, C.-C. Hsu, C.-W. Lai, C.-C. Hsieh, S. H. Lin, Y.-M. Cheng, and P.-T. Chou, "The empirical correlation between size and two-photon absorption cross section of CdSe and CdTe quantum dots," Small **2**, 1308-1313 (2006).
25. M. J. Levene, D. A. Dombeck, K. A. Kasischke, R. P. Molloy, and W. W. Webb, "In vivo multiphoton microscopy of deep brain tissue," J. Neurophysiol. **91**, 1908-1912 (2004).
26. F. Chen, and D. Gerion, "Fluorescent CdSe/ZnS nanocrystal-peptide conjugates for long-term, nontoxic imaging and nuclear targeting in living cells," Nano Lett. **4**, 1827-1832 (2004).
27. J. G. D. Foley, and J. B. L. Bard, "Apoptosis in the cortex of the developing mouse kidney," J. Anat. **201**, 477-484 (2002).
28. W. Jiang, A. Singhal, J. Zheng, C. Wang, and W. C. W. Chan, "Optimizing the synthesis of red- to near-IR-emitting CdS-capped $CdTe_xSe_{1-x}$ alloyed quantum dots for biomedical imaging," Chem. Mater. **18**, 4845-4854 (2006).
29. I. Nabiev, S. Mitchell, A. Davies, Y. Williams, D. Kelleher, R. Moore, Y. K. Gun'ko, S. Byrne, Y. P. Rakovich, J. F. Donegan, A. Sukhanova, J. Conroy, D. Cottell, N. Gaponik, A. Rogach, and Y. Volkov, "Nonfunctionalized nanocrystals can exploit a cell's active transport machinery delivering them to specific nuclear and cytoplasmic compartments," Nano Lett. **7**, 3452-3461 (2007).
30. Y. Xu, Q. Wang, P. He, Q. Dong, F. Liu, Y. Liu, L. Lin, H. Yan, and X. Zhao, "Cell nucleus penetration by quantum dots induced by nuclear staining organic fluorophore and UV-irradiation," Adv. Mater. **20**, 3468-3473 (2008).
31. K.-T. Yong, I. Roy, H. E. Pudavar, E. J. Bergey, K. M. Tramposch, M. T. Swihart, and P. N. Prasad, "Multiplex imaging of pancreatic cancer cells by using functionalized quantum rods," Adv. Mater. **20**, 1412-1417 (2008).
32. L. Wang, D. Ancukiewicz, J. Y. Chen, and R. K. Jain, "Surface-plasmon enhanced fluorescence in CdSe/ZnS semiconductor quantum dots," Paper # CTu07, presented at the Conference on Lasers and Electro-Optics Conference (CLEO/IQEC 2009), Baltimore, MD, 31 May, 2009
33. All the SQD samples described here were purchased from Evident Technologies; the "2 nm" USQD samples used in this study are their "Blue" product with a specified CdSe core diameter of 1.9 nm (+/- 5%) and a peak emission wavelength of 490 nm, consistent with our measurements reported here.
34. Z. Tang, N. A. Kotov, and M. Giersig, "Spontaneous organization of single CdTe nanoparticles into luminescent nanowires," Science **297**, 237-240 (2002).
35. K. I. Kang, B. P. McGinnis, Sandalphon, Y. Z. Hu, S. W. Koch, N. Peyghambarian, A. Mysyrowicz, L. C. Liu, and S. H. Risbud, "Confinement-induced valence-band mixing in CdS quantum dots observed by two-photon spectroscopy," Phys. Rev. B **45**, 3465-3468 (1992).
36. M. E. Schmidt, S. A. Blanton, M. A. Hines, and P. Guyot-Sionnest, "Size-dependent two-photon excitation spectroscopy of CdSe nanocrystals," Phys. Rev. B **53**, 12629-12632 (1996).
37. A. L. Efros, and M. Rosen, "Electronic structure of semiconductor nanocrystals," Annu. Rev. Mater. Sci. **30**, 475-521 (2000).
38. N. J. Durr, T. Larson, D. K. Smith, B. A. Korgel, K. Sokolov, and A. Ben-Yakar, "Two-photon luminescence imaging of cancer cells using molecularly targeted gold nanorods," Nano Lett. **7**, 941-945 (2007).
39. B. I. Tarnowski, F. G. Spinale, and J. H. Nicholson, "DAPI as a useful stain for nuclear quantitation," Biotech. Histochem. **66**, 296-302 (1991).
40. H. M. Elsheikha, and L. S. Mansfield, "Assessment of Sarcocystis neurona sporocyst viability and differentiation between viable and nonviable sporocysts using propidium iodide stain," J. Parasitol. **90**, 872-875 (2004).
41. C. Xu, and W. W. Webb, "Measurement of two-photon excitation cross sections of molecular fluorophores with data from 690 to 1050 nm," J. Opt. Soc. Am. B **13**, 481-491 (1996).

---

1. Background and Need

Multiphoton absorption, particularly two-photon absorption (TPA), followed by fluorescence, has been identified as a useful technique for deep tissue imaging [1-3] for the study of several biological and biomedical processes, such as optical biopsy of *in vivo* human skin [2], angiography [4], embryonic development in hamsters [5], intravital measurement of gene expression in mice tumors [6], and intravital studies of mouse and rat brains [7, 8] and kidneys [9]. The advantages of two-photon absorption-induced fluorescence (TPAF) imaging stem not only from the larger depths of penetration [10, 11] that are obtainable at the longer wavelengths inevitably used for excitation, but also from the ease of filtering the near-IR TPAF excitation from the visible or near-UV fluorescence emission, and the higher spatial resolutions inherent in multiphoton microscopy [12].

For tissue specimens in which the use of labeling is necessary, the use of semiconductor quantum dots (SQDs) as biological labels [13, 14] – in comparison with fluorescent dyes [15] – is particularly desirable because of (i) their photochemical stability [16], (ii) their ability to be tuned over broad wavelength ranges [17], and (iii) their amenability to bio-conjugation [18-22]. Several researchers [4, 23, 24] have also demonstrated that SQDs exhibit very large TPA coefficients, particularly in comparison to those of dyes used for TPAF-based imaging. In most previous studies using SQDs for TPAF imaging of biological tissues [4, 25], relatively large SQDs (diameter $d \geq 5$ nm) have been used because their TPA coefficients are much larger those of smaller SQDs of the same material

composition [24]. In particular, Larson et al [4] have demonstrated that the two-photon "action cross-sections" (product of the TPA cross section and the fluorescence quantum efficiencies) of CdSe/ZnS SQDs are over 3 orders of magnitude higher than those of conventional dye-based fluorescent probes (such as fluorescein isothiocyanate (FITC)-dextran), with measured values as high as 47,000 Goeppert -Mayer (GM) units. These authors also demonstrated visualization of capillaries hundreds of micrometers deep through the skin of living mice with such SQD-based TPAF probes.

In addition, even though most of the studies of bio-imaging based on quantum dot labels have used relatively large SQDs ($d \geq 5$ nm) [4, 14, 25-31], there are numerous biological imaging studies in which the use of much smaller SQDs is critical. These include deep-tissue wavelength-multiplexed multicolor imaging [28, 31] in which smaller SQDs of the same material lead to fluorescence at shorter wavelengths ("bluer") and applications involving intra-nuclear studies of cells [26, 27, 29, 30] *in which much smaller SQDs are critical for effective penetration of the sub-10 nm nuclear pores [30]*.

2. Proposed Solution and Summary of Results

Unfortunately, smaller SQDs usually lead to weaker TPAF signals (because of their smaller TPA coefficients). *It is thus critical to maximize the output signals from smaller SQDs for their effective use in biological imaging applications*. This can be done by: (a) using semiconductor materials with relatively high intrinsic quantum efficiencies, (b) optimizing the size of such quantum dots to obtain emission wavelengths that coincide with the presence of efficient photomultiplier or photodetector systems, (c) enhancing the TPAF signals via use of appropriate methods of plasmonic enhancement, such as that enabled by appropriately-designed SQD-gold nanoparticle assemblies [32], and (d) *optimizing the choice of the excitation wavelengths for SQDs chosen in accordance with the first two factors*. Even though the first two factors have been studied considerably in previous studies of linear fluorescence and TPAF from SQDs, the last two -- namely the issue of optimization of the excitation wavelength and that of plasmonic enhancement -- have not been explored adequately, particularly for the use of small or ultrasmall SQDs for biological imaging applications. Based on these factors and available data on SQD emission wavelengths and efficiencies, we propose the use of ultrasmall (≤ 2 nm) CdSe/ZnS SQDs for the specialized (intra-nuclear and multicolor) biomedical imaging applications mentioned above, *and describe a detailed study on the excitation wavelength dependence of the fluorescence emission from such ultrasmall (≤ 2 nm) semiconductor quantum dots (USQDs) at room temperature, which is particularly relevant to the biomedical imaging applications of interest*. In particular, in this paper, we demonstrate strong resonant enhancement of the TPAF signal for 2 nm CdSe/ZnS USQDs at wavelengths and intensities that are readily achievable from relatively standard commercial Ti-sapphire laser systems; at a "nominal" intensity of 8 GW/cm^2, the TPAF signals at excitation wavelengths near 780 nm were observed to be ~ 8 times larger than those at 850 nm and ~ 68 times larger than those at 900 nm, *indicating that this USQD system appears highly relevant for use in future biological imaging studies, particularly for multicolor imaging and nuclear penetration studies (such as those utilized for studies of cell apoptosis)*.

3. Experimental Setup and Related Details

A mode-locked Ti-sapphire laser of 200 fs pulsewidth and 76 MHz repetition rate was used as the excitation source to characterize the TPAF signals. As shown in Fig. 1, a concave mirror of 10 cm focal length was used to focus the 2 mm diameter laser beam to a spot size of 80 μm into a colloidal USQD suspension ("sample") placed in a cuvette of 2 mm pathlength.

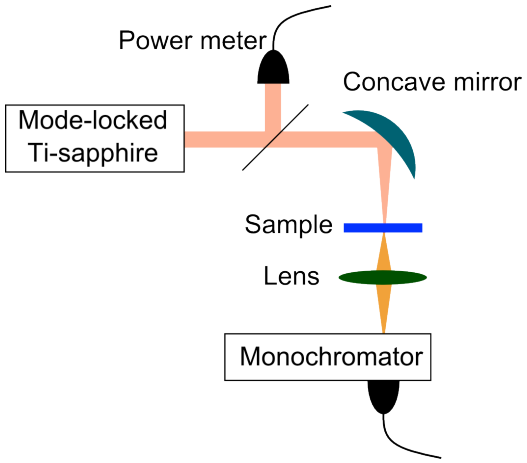

Fig. 1. Experimental setup used to characterize TPAF signals from CdSe/ZnS USQDs.

Standard lock-in detection techniques were used to measure the TPAF signals collected by a photomultiplier tube (PMT) at the exit port of a half-meter monochromator with a slit width of 2 mm, corresponding to a spectral resolution of ~ 3 nm. For this study, we used CdSe/ZnS (core/shell) USQDs of core diameter d ~ 2 nm in toluene, with a specified size variation of less than 5%; the total physical diameter of the USQDs is ~ 3.2 nm when ZnS shell are also taken into account [33].

4. Results and Discussion

In order to interpret the TPAF data (taken with the experimental setup of Fig. 1) accurately, it is important to characterize the USQD samples in terms of their "baseline" linear optical and physical properties. The single photon absorption spectrum of these USQDs is shown in Fig. 2(a), with a peak at ~ 460 nm and a full width at half maximum (FWHM) of ~ 40 nm. Also as seen in Fig. 2(a), the linear fluorescence spectrum exhibits a peak emission wavelength of ~ 496 nm and a FWHM of ~ 30 nm. This emission spectrum was obtained by using either a 325 nm He-Cd laser or the second harmonic generation of our mode-locked Ti-sapphire laser as the excitation source, and no significant difference was noted in the emission spectra for these two excitation sources. The peak locations of these spectra are consistent with those expected [33] from CdSe SQDs with a core diameter of 2 nm, and the FWHMs of these spectra confirm a size variation of less than 5% and the absence of aggregation [34] in these USQD samples. It is useful to note that no significant changes in the spectra -- nor any other sign of aggregation -- was noted even after these USQD samples were stored in the lab at room temperature for over a month.

We also examined these USQD samples with a transmission electron microscope (TEM). A typical TEM image is shown in Fig. 2(b); in this image, the darker spots correspond to individual SQDs. Because of the lack of sufficient resolution and the low contrast in these TEM images (typical with CdSe/ZnS SQDs), it was difficult to accurately resolve the exact size of our SQDs. Nevertheless, it is easy to estimate an upper limit of about 4 nm for the "particles" (darker dots) seen more predominantly in the lower right quadrant of these TEM images, and to confirm the general lack of aggregation of these particles. Note that the "sub-nm" type of finer grain structure seen in this TEM image is an artifact of the imaging setup. The fact that the darker dots were not artifacts of our TEM imaging setup, and corresponded to the anticipated quantum dots was verified with an XRD analysis; the data from this analysis confirmed the existence of all the anticipated elemental compounds (Cd, Se, Zn, S).

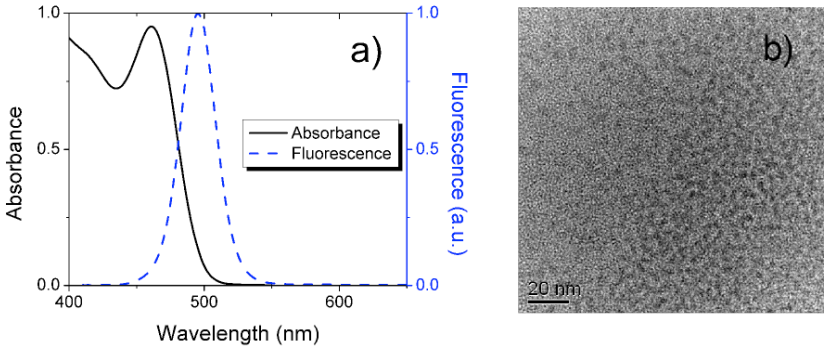

Fig. 2. (a) Linear absorption (peak at 460 nm and FWHM of 40 nm) and fluorescence (peak at ~ 496 nm and FWHM of 30 nm) spectra of 2 nm CdSe/ZnS USQDs. The absorbance corresponds to a 2 mm path length solution at a concentration of 1.4 mg/ml; (b) a typical TEM image of the CdSe/ZnS USQDs used in this study. The darker dots that are predominantly in the lower left hand area (below the NE to SW diagonal) are the CdSe SQDs, whereas the finer "sub-nm" type of graininess in the image is due to an artifact of the TEM imaging setup.

Note that the emission spectra from the ZnS shell (peak wavelength > 335 nm) and the capping layer are both located at wavelengths far from the emission spectra of the CdSe USQDs. Nevertheless, in order to confirm that the ZnS and capping layers provide negligible amounts of contribution to the CdSe USQD emission spectrum of Fig. 2(a), we studied the emission spectra from a range of CdSe/ZnS SQD samples containing dots of varying sizes, as shown in Fig. 3 below. Any emission from the ZnS shell and capping layers would show up as an extraneous "common" feature in each of these spectra; the lack of any such common emission spectrum confirms the absence of any interfering emission from the ZnS shell and the capping layers in this spectral region.

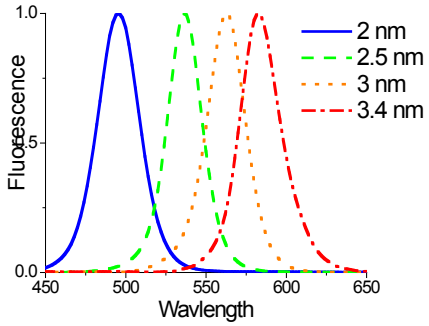

Fig. 3. Linear fluorescence from four different CdSe/ZnS SQD colloidal samples, corresponding to SQDs of distinct average sizes varying from 2 nm to 3.4 nm

We next used the experimental setup of Fig. 1 to measure TPAF spectra for several distinct excitation wavelengths in the 750 nm to 950 nm range while keeping the excitation intensity constant (~ 8 GW/cm^2). Six representative spectra in the 810 nm to 860 nm range are shown in Fig. 4. The spectral shapes and the peak wavelengths of the TPAF emission spectra were very similar to those observed with single photon excitation, and showed a negligible change (≤ 5%) as a function of the excitation wavelength.

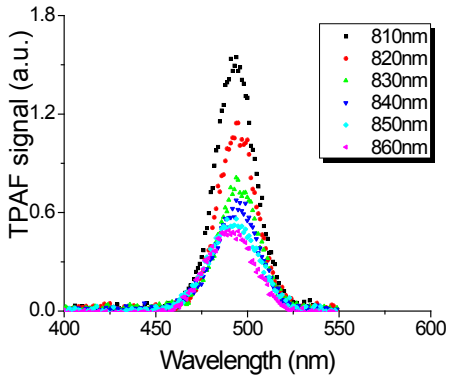

Fig. 4. TPAF spectra for several distinct excitation wavelengths in the 810 nm - 860 nm range, using a constant excitation intensity of 8 GW/cm^2. The vertical axis corresponds to the signals obtained with the lock-in amplifier when the PMT is located at the exit of the monochromator.

In order to verify that the observed fluorescence emission was caused by a two-photon absorption process, we measured the dependence of the fluorescence power on the excitation intensity (Fig. 5). This was done by removing the monochromator and measuring the power in the entire spectrum ("area under the curve") at the photomultiplier, while introducing a short-pass optical filter (Schott BG 39) to block any contributions to the PMT signal from any stray scattered light from the Ti-sapphire laser. Log-log plots of the fluorescence power ("TPAF signal") as a function of the excitation intensity are shown in Fig. 5 for two representative wavelengths, 810 nm (dots) and 930 nm (triangles). The slopes of the fitting lines (dashed for 810 nm and solid for 930 nm) are 2.0 (+/-0.15) and 1.9 (+/-0.15), confirming that the measured fluorescence emission was caused by a TPA process.

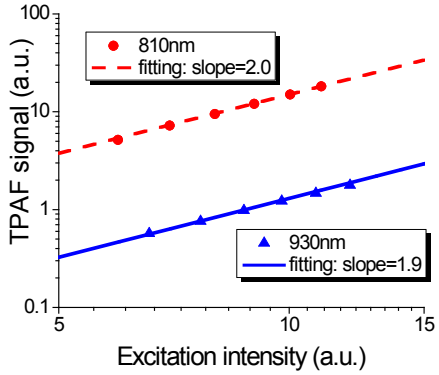

Fig. 5. Power in the TPA-induced fluorescence as a function of the excitation intensity for excitation at 810 nm and 930 nm respectively. The vertical axis corresponds to the lock-in amplifier signal when the entire fluorescence spectrum (no monochromator) is focused on the PMT, and a value of 12 on the horizontal axis corresponds to an intensity of ~ 8 GW/cm^2.

We next measured the "integrated" (over the entire emission spectrum) optical power in the TPAF emission as a function of the excitation wavelength while keeping the excitation intensity at each excitation wavelength constant (at 8 GW/cm^2). Fig. 6 shows the result of such measurements for two different SQD concentrations (1.4 mg/mL and 0.4 mg/mL of CdSe). These plots depict strong resonant enhancement in the TPAF signals at excitation wavelengths close to 780 nm; for the more concentrated sample, the TPAF signal at 780 nm is ~ 8 times that at 850 nm and ~ 68 times that at 900 nm. Note that when the experiment was

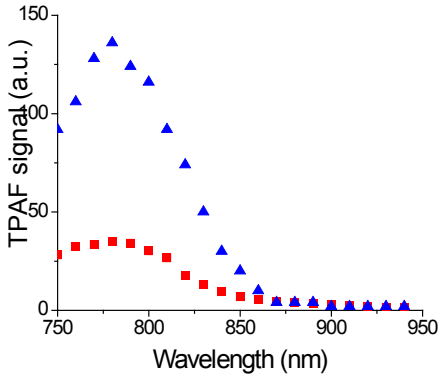

Fig. 6. The wavelength dependence of the TPA-induced fluorescence outputs for the 2 nm CdSe/ZnS USQDs at two different concentrations (1.4 mg/mL: blue triangles; 0.4 mg/mL: red squares).

repeated with just the solvent (without any SQDs therein), there was no measurable fluorescence, indicating that there was no "background" fluorescence attributable to the solvent, and the measured TPAF signals are entirely due to the USQDs themselves. Note also that although lower USQD concentrations may be preferred for some biological studies, the higher concentration (1.4 mg/ml) is within the range of concentrations that may be usable for several biological imaging experiments. Nevertheless, ***these experiments clearly illustrate that with these USQDs for TPAF-based deep-tissue imaging, the use of an excitation wavelength of 780 nm is optimal, with signal enhancements as much as 68 times over those obtained at an excitation wavelength of 900 nm.*** Note also that most tissue of interest is highly transparent at 780 nm, and that this wavelength is still conducive to high-resolution deep-tissue imaging.

It is interesting to note that the excitation wavelength at the TPAF peak is not exactly twice of the peak wavelength for linear absorption: the TPAF peak is observed to occur at about 780 nm, which is shorter than that expected based on the peak wavelength (~ 460 nm) of the linear absorption. Such a wavelength difference can be accounted for by considering the role of different transitions and selection rules associated with single photon absorption and TPA. It is well known that the selection rules are different for single photon absorption and TPA in semiconductor interband transitions [35]: single photon transitions satisfy $\Delta L = 0, \pm 2$ and $\Delta F = 0, \pm 1$ and two-photon transitions satisfy $\Delta L = \pm 1, \pm 3$ and $\Delta F = 0, \pm 1, \pm 2$ (where F is the total angular momentum). Although such selection rules are not strictly followed in USQDs because of band-mixing effects, the magnitude of the cross sections might still differ significantly, i.e., TPA transitions with $\Delta L = \pm 1, \pm 3$ and $\Delta F = 0, \pm 1, \pm 2$ have much larger cross sections than those with $\Delta L = 0, \pm 2$ and $\Delta F = 0, \pm 1$ [36].

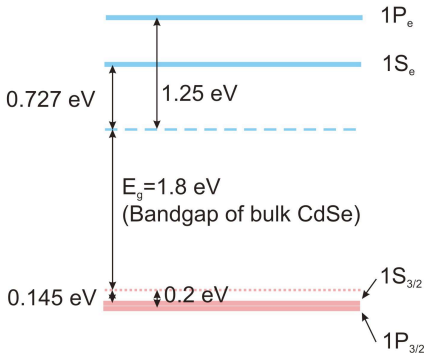

Fig. 7. Schematic of the electronic energy levels for CdSe/ZnS quantum dots of 2 nm diameter. (see ref [37] for details)

To identify the energy levels inside this particular USQD system (λ_{abs} = 460 nm), an 8-band Pidgeon & Brown model was employed to calculate the energy levels positions [37]. Fig. 7 schematically shows the lowest two levels in the conduction and valence bands. The bandgap of bulk semiconductor CdSe is 1.8 eV, with the dashed blue and the dotted red lines indicating the bottom of the conduction band and the top of the valence band, respectively. The

two hole energy levels closest to the band edge are $1S_{3/2}$ (0.145 eV below the band edge) and $1P_{3/2}$ (0.2 eV below the band edge), and the two electron energy levels closest to the band edge are $1S_e$ (0.727 eV above the band edge) and $1P_e$ (1.25 eV above the band edge), respectively. Thus the transition $1S_{3/2} \Rightarrow 1S_e$ gives the lowest single photon peak absorption energy (2.672 eV or 464 nm), which matches our experimental data (460 nm: peak absorption wavelength for single photon excitation) quite well, while the transition $1S_{3/2} \Rightarrow 1P_e$ corresponds to a TPA photon energy (3.195 eV or 776 nm for TPA) that also matches our experimental data (780 nm wavelength of the TPA peak) well.

One potential problem of using USQDs in biomedical imaging applications is that the emission spectrum may be too close to or may even overlap with that of autofluorescence in tissues. Fortunately, the TPAF signals from SQDs are much stronger than the TPA signals from autofluorescence in tissues. The TPA cross sections of SQDs can be as high as 47,000 GM units [4], and the TPA cross sections estimated for our USQDs are ~ 7,000 GM units based on an open aperture z-scan measurement, while the TPA cross sections for autofluorescence in tissues are only of the order of a few GM [38].

5. Summary and Future Plans

We have proposed the use of USQDs for various deep-tissue biological imaging applications, notably wavelength-multiplexed multicolor imaging and intra-nuclear studies such as those involving cell apoptosis, and have studied the issue of maximizing TPAF signals from CdSe/ZnS USQDs to be used for this application. In particular, using 2 nm USQDs, we have shown that the TPAF signal at 780 nm is ~ 8 times that at 850 nm and 68 times that at 900 nm, two wavelengths that have been used in previous studies using CdSe/ZnS SQDs for deep-tissue imaging of biological studies via TPAF [4].

We plan to extend these studies in the near future to the assessment of cell apoptosis in the cortex of mice kidneys, since these organs are near-standard "baseline" subjects for cell apoptosis studies via other methods [9]. Although large fluorescence signals are expected from larger SQDs, their limited ability for nuclear penetration is expected to hamper the type of data that is critically needed for cell apoptosis studies. We have started experiments on the permeation of USQDs into cell nuclei and other tissues; once this has been achieved, we will compare results obtained by TPAF using traditional dyes and SQDs with the results obtained by USQDs. The signals anticipated for the USQDs proposed here are expected to be several orders of magnitude stronger than those obtainable from the most efficient dyes (DAPI [39] and propidium iodide [40]) relevant for TPAF studies in this wavelength range [41].

Acknowledgements

We thank Prof. Kevin Malloy for the use of his mode-locked Ti-sapphire laser for some of the preliminary data related to these studies. We also thank Weiliang Chen and Melissa Aillaud for their assistance in experiments related to this study. This work was supported by the US Department of Energy (Grant # DE-FG02-02ER46015) and the Air Force Office of Scientific Research (Grant # FA9550-06-1-0001).

Appendix B: Surface-Plasmon Enhanced Fluorescence in CdSe/ZnS Semiconductor Quantum Dots

L. Wang[1], D. Ankuciwiez[2], J. Y. Chen[1], and R. K. Jain[1]
[1]*Center for High Technology Materials, University of New Mexico, 1313 Goddard St SE, Albuquerque, NM 87106*
[2]*Applied Physics, Columbia University, 500 W. 120th Street, New York, NY 10027*
liwang@chtm.unm.edu

Abstract: We report surface-plasmon enhanced fluorescence in CdSe/ZnS semiconductor quantum dots via linear and nonlinear excitations. 2x and 10x fluorescence enhancements have been achieved for linear and nonlinear excitations, respectively.

OCIS codes: (170.6280) Spectroscopy, fluorescence and luminescence; (240.6680) Surface plasmons

Surface plasmons (SPs) are quantizations of oscillations in the electric field and charge distribution. Excitation of surface plasmons within metal nanoparticles (dimension of 5 – 100 nm) can create strong local optical fields. Surface-enhanced Raman scattering (SERS) has used such strong fields to achieve fluorescence enhancement factor over 10^{13} in organic molecules. Semiconductor quantum dots (SQDs) exhibit significant advantages over fluorescence dyes due to their: (a) broader absorption spectra and more readily tunable emission options (b) higher quantum yields, and (c) higher photochemical stability. However, the interactions between SPs and SQDs are still relatively poorly understood. Experiments-to-date give contradictory results on detailed issues that affect fluorescence enhancements [1, 2]. Detailed parametric studies of linear (excitation photon energy > bandgap of SQDs) and nonlinear (excitation photon energy < bandgap of SQDs) fluorescence enhancements in SQDs are srongly needed.

Nonlinear fluorescence (such as two-photon absorption-induced) has been identified as a useful technique for bio-imaging (mediated by fluorescence signatures) for the study of several biological processes, such as angiography and optical biopsy [3] of in vivo human skin [4]. Enhanced nonlinear fluorescence will greatly benefit such bio-imaging applications if SQDs and metal nanoparticles are bundled together with controlled spacings. Ma et al. [5] have demonstrated 6x fluorescence enhancement in Au:CdS composite thin films, however it is hard to quantitatively describe the interactions with randomly distributed CdS nanocrystals and Au nanoparticles. Controlled samples with well-defined spacings between the SQDs and the metal nanoparticles are critical for this study.

Arrays of SQDs and Au nanoparticles (nanospheres for linear and nanorods for nonlinear experiments) were built to obtain controllable samples. First, ~ 5 nm diameter CdSe/ZnS quantum dots (absorption peak 522 nm) were spin-coated onto a glass slide. Next, a 10 nm spacer layer of SiO_2 was deposited on top of the previous layer using evaporative deposition. Finally, a layer of gold nanospheres was deposited by putting a droplet of Au nanospheres in ethanol solution on the desired surface and evaporating the solvent quickly. Fig. 1 shows an SEM micrograph of such a deposited layer (50 nm Au nanospheres). It is clear that the gold nanospheres are almost evenly distributed on one layer.

The samples were excited with the second-harmonic generation (400 nm) of a mode-locked Ti-sapphire laser, and fluorescence spectra were measured using a ½-meter monochromator (CVI Digikrom 480), a photomultiplier tube (Hamamatsu R928) and a lock-in amplifier (Stanford Research Systems SR830). Fig. 2 shows fluorescence spectra of the SQDs with and without the Au nanosphere layer. An approximately two-fold increase in fluorescence intensity is evident. The blue-shift of the enhanced fluorescence spectrum is presumably related to the resonant plasmon frequency of 50 nm Au nanospheres (~ 520 nm). Phase fluorimetry [6] was used to measure the fluorescence rates in order to verify enhancement. A blue (465 nm) light-emitting diode (LED) was modulated at frequencies of 1-5 MHz, and the phase shift between the modulated excitation light and the resulting fluorescence was used to calculate the fluorescence rate. Preliminary phase fluorimetry results indicate that the fluorescence rate of the quantum dots increased from approximately $8 \cdot 10^7$ s^{-1} to approximately $13 \cdot 10^7$ s^{-1}, presumably due to increased coupling to the Au nanospheres.

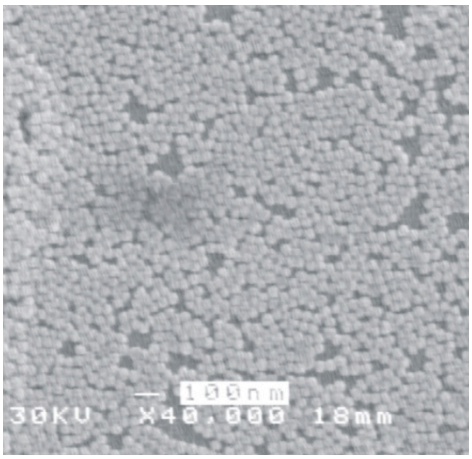

Fig. 1. SEM micrograph of a 50 nm Au nanoparticle layer deposited by a droplet evaporation method

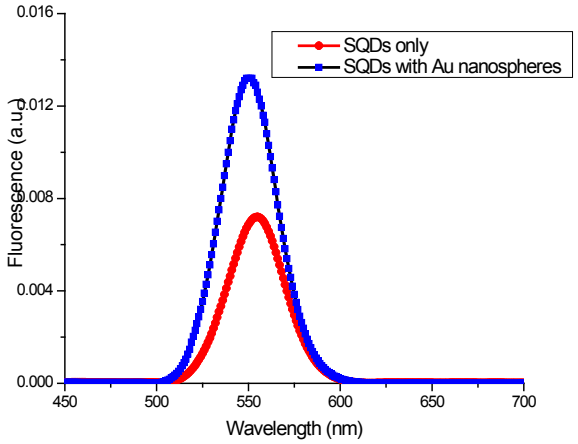

Fig. 2. Linear fluorescence spectra of 522 nm CdSe/ZnS SQDs with and without 50 nm Au nanoparticles, there is a 10 nm spacer layer between the QDs and the Au nanospheres.

A mode-locked Ti-sapphire laser (~ 800 nm) was used to excite the samples in nonlinear fluorescence studies. Similar samples were prepared with Au nanorods (plasmon frequency ~ 750 nm, 25 nm cross-section diameter) to match the excitation wavelength with the resonant plasmon frequency of the Au nanorods. Preliminary results have shown a 10x enhancement of fluorescence, as shown in Fig. 3. Further experiments with different SQDs sizes and SiO_2 spacer thicknesses are in progress to investigate the factors that affect such linear and nonlinear processes and to optimize the parameters for maximum enhancement.

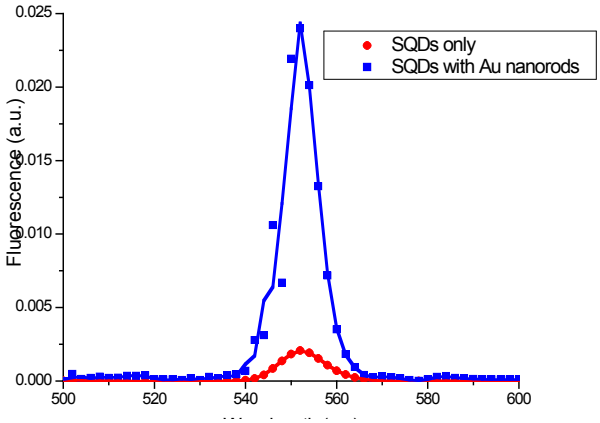

Fig. 3. Nonlinear fluorescence spectra of 522 nm CdSe/ZnS SQDs with and without Au nanorods, there is a 10 nm spacer layer between the QDs and the Au nanorods.

References:

[1] Z. Gueroui and A. Libchaber, "Single-molecule measurements of gold-quenched quantum dots," Phys. Rev. Lett. **93**, 166108 (2004)

[2] J. H. Song, T. Atay, S. F. Shi, H. Urabe and A. V. Nurmikko, "Large enhancement of fluorescence efficiency from CdSe/ZnS quantum dots induced by resonant coupling to spatially controlled surface plasmons," Nano Lett. **5**, 1557 (2005)

[3] D. R. Larson, W. R. Zipfel, R. M. Williams, S. W. Clark, M. P. Bruchez, F. W. Wise, and W. W. Webb, "Water-soluble quantum dots for multiphoton fluorescence imaging in vivo" Science **300**, 1434 (2003).

[4] B. R. Masters, P. T.C. So, and E. Gratton, "Optical biopsy of in vivo human skin: multi-photon excitation microscopy," Laser Med. Sci. **13**, 196 (1998).

[5] G. H. Ma, J. He, K. Rajiv, S. H. Tang, Y. Yang and M. Nogami, "Observation of resonant energy transfer in Au:CdS nanocomposite," Appl. Phys. Lett. **84**, 4684 (2004)

[6] E. A. Bailey, Jr. and G. K. Rollefson, "The determination of the fluorescence lifetimes of dissolved substances by a phase shift method," J. Chem. Phys. **21**, 1315 (1953)

Appendix C: Surface Plasmon Assisted Broadband Emission from Nanostructured Metal-Insulator-Metal Tunnel Junctions

J. Y. Chen, D. Ancukiewicz, L. Wang and R. K. Jain
Center for High Technology Materials, University of New Mexico, 1313 Goddard SE, Albuquerque NM 87106
jychen@chtm.unm.edu

jain@chtm.unm.edu

Abstract: We report the observation of double-peaked broadband emission from nanostructured Al-Al_2O_3-Au tunnel junctions at high applied voltages. We argue that it results from an interaction with surface plasmons excited at metal-air interface.

OCIS codes: (130.0250) Optoelectronics; (240.6680) Surface plasmons; (240.0310) Thin films

1. Introduction

An enhanced electron tunneling can be achieved through plasmon excitation in tunnel junctions (TJs) [1] and based on this light emission from TJs has been demonstrated previously [2-3]. Since then several experimental and theoretical studies have been done to explain this phenomenon [4-7]. It is generally agreed that the emission results from coupling between surface plasmon (SP) and photon at the metal-air interface through surface discontinuities.

In this paper, we report the observation of comparatively uniform broadband light emission with spectrum extending from visible (around 550nm) to near-IR (around 850nm) from Al-Al_2O_3-Au tunnel junctions fabricated on gratings. The near-IR emission was not observed from junctions fabricated on glass slides at low applied voltages, but appeared when the applied voltages exceeded 4.1V.

2. Experiments

Our tunnel junctions are prepared by thermal evaporation on different sublayers including microscope glass slides, MgF_2 films and periodic gratings. The MgF_2 film is directly deposited onto the glass slides with a thickness around 200nm. The grating has a period of 800nm and amplitude of 100nm. Onto the sublayers an Al film is deposited as the bottom electrode (cathode) of the junction and the thickness is usually greater than 100nm. The Al layer is then thermally oxidized at 200°C for 2 hours and covered with a 25-nm-thick Au film as the top electrode (anode) of the junction.

The junction has an area around $4mm^2$ and a typical resistance about 200Ω with DC applied voltage at 3.0V. The oxide layer thickness is around 3.5nm by a capacitance fitting. All the measurements are operated at room temperatures.

During the measurements, the tunnel junction is mounted onto a translation stage, and then a focusing lens is used to launch the emitted light into the monochromator, which is then connected to a photomultiplier tube. A

photon counting system is employed for easier measurements and the signal out there is sent into computer for records.

3. Results and Discussions

Fig. 1 shows emission spectra from junctions fabricated directly on glass slides measured at voltages varying from 3.9V to 4.1V. The spectra at 3.9V and 4.0V are similar, but the spectrum obtained at 4.1V differs from the previous two with much higher emission intensity, a significantly elevated near-IR peak and a slight wavelength shift of the visible emission towards longer wavelengths. Although it is not shown here, this near-IR emission was still observed when we reduced the applied voltage from 4.1V back to 3.9V, which indicates that some permanent changes have been made on the device structure. This is confirmed by studying the junction surfaces with an optical microscope, as shown in Fig. 3. The junction surface before measurements is much smoother than after the measurements. This roughened surface can explain the increased emission intensity that is related to the surface diffraction efficiency and then scales proportionally with the mean-square surface roughness [6]. Meanwhile, the surface mophology has also been changed, which results in a decrease in surface correlation length, as shown in Fig. 3. Qualitatively speaking, this decrease in surface correlation length leads to decreased light wavevector coupled from surface plasmon, which corresponds to the near-IR emission not seen at low applied voltages.

Fig. 2 shows the comparison of emission spectra from tunnel junctions fabricated on a smooth glass slide, MgF_2 film and a periodic grating (of period a = 800nm as mentioned earlier), respectively. While the first (on glass slide) is measured at 4.0V, the latter two are measured at 3.5V and still exhibit much higher emission intensities. Again this should result from the difference in surface roughness scales. No near-IR emission is observed from junctions on MgF_2 because no appropriate surface discontinuity is available to make up for the wavevector difference between SP and light in that wavelength range. This result agrees with the theoretical work of Laks and Mills [7]. The emission spectrum from the junction fabricated on a periodic grating has comparable visible emission intensity to that of junction on MgF_2, and a much higher emission peak in near-IR region. There is little chance that this significantly elevated 800nm emission peak is caused by decay of high-energy photons, since such near-IR emission is not obviously observed from junction fabricated on MgF_2 layer, which exhibits at least comparable emission intensity in visible range. This elevated near-IR emission is more likely the result of near-IR surface plasmons being selectively coupled out with light by gratings based on the following equation (1), where *a* is the grating period; n indicates the grating order and can be different natural numbers; θ is the angle between junction surface and couplied light; K_l is the free space light wavevector and K_{sp} is the surface plasmon wavevector excited by Al-Al_2O_3-Au junctions [8]. The calculation shows that the 800nm gratings make up for the wavevector difference between free space light and Au fast-mode surface plasmons. It should be noted that there is no control on the direction of coupled light and our measurements are not for a specific angle, which results in the spectrum extending from 550nm to 850nm.

$$K_l \sin\theta = K_{sp} - n \cdot \frac{2\pi}{a} \qquad (1)$$

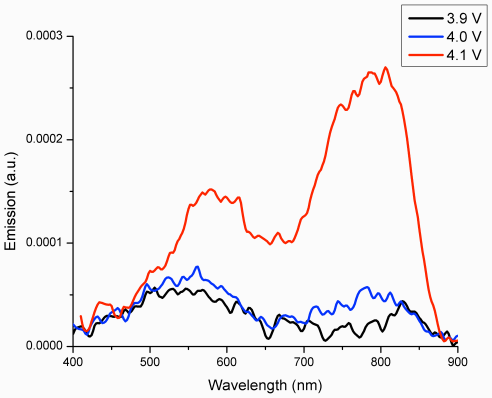

Fig. 1: Emission spectra from the tunnel junction fabricated on a glass slide with different DC applied voltages

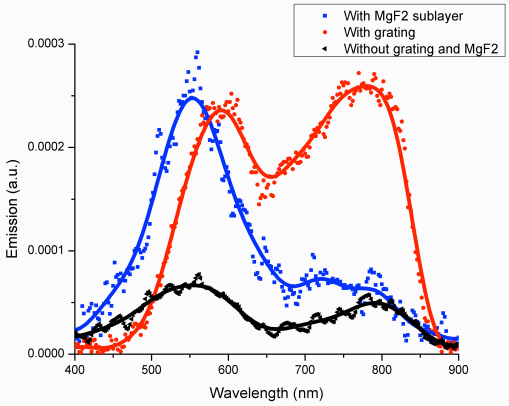

Fig.2: Emission spectra from tunnel junctions fabricated on glass slide, MgF_2 and grating respectively

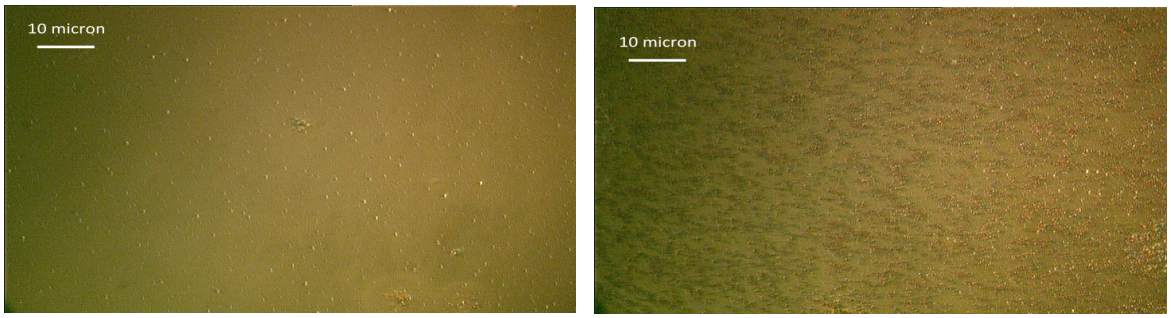

Fig. 3: Images of junction surface (a) before and (b) after spectral measurement

Also it is noticed that the original spectrum shifts to lower energy when the near-IR emission appears. The mechnism is not yet totally understood, but this might be related to the increase of surface roughness [5].

The device can work stably at 3.5V for one hour under room temperature, but breaks down much more easily when applied voltage is increased above 4V, most likely due to the dielectric breakdown that occurs when the electric field exceeds 10^9 V/m in aluminum oxide [9].

4. Future Work

Based on the achieved broadband emission, we would like to next improve the emision efficiency by introducing quantum dots. Previous results shown that the tunnel junction is a compact yet efficient hot electron generator, and these hot electrons can be used to excite quantum dots efficiently provided that their kinetic energies are three times or higher of the band-gap energy [10]. This will require a more reliable oxide layer that can withstand an applied voltage around 10V. Then a metal-insulator-semiconductor tunneling structure might be employed instead of metal-insulator-metal structures, where the quantum dots can be embedded into the semiconductor layer and the oxide layer will behave not only as a barrier, but also a spacer between metal and quantum dots to avoid quenching.

With quantum dots introduced, we will expect two mechanisms that will contribute to the light emission: surface plasmon assisted emission and direct radiative recombination. When electrons tunnel into the semiconductor layer, the quantum dots will be excited, and the excitons can decay radiatively or nonradiatively [11]. The radiative decay will lead to the direct emission, while part of the nonradiative decay will be into surface plasmon and can be exploited to generate a second emission provided that surface roughness is available to make up for the wavevector difference. The estimated efficiency is at least one order of magnitude higher than that without quantum dots.

5. References

[1] D. P. Siu, R. K. Jain and T. K. Gustafson, "Stimulated electron tunneling in metal-barrier-metal structures due to surface plasmons," Appl. Phys. Lett. 28, 407-410 (1976)
[2] T. L. Hwang, S. E. Schwarz and R. K. Jain, "Plasma radiation from tunnel junctions," Phys. Rev. Lett. 36, 379-382 (1976).
[3] J. Lambe and S. L. McCarthy, "Light emission from inelastic electron tunneling," Phys. Rev. Lett. 37, 923-925 (1976).
[4] R. K. Jain, S. Wagner and D. H. Olson, "Stable room-temperature light emission from metal-insulator-metal junctions," Appl. Phys. Lett. 32, 62-64 (1977).
[5] J. Kirtley, T. N. Theis and J. C. Tsang, "Light emission from tunnel junctions on gratings," Phys. Rev. B 24, 5650-5663 (1981).
[6] B. Laks and D. L. Mills, "Roughness and the mean free path of surface polaritons in tunnel-junction structures," Phys. Rev. B 21, 5175-5184 (1979).
[7] B. Laks and D. L. Mills, "Photon emission from slightly roughened tunnel junctions," Phys. Rev. B 20, 4962-4980 (1979).
[8] P. D. Sparks and J. E. Rutledge, "Light emission from random rough tunnel junctions," Phys. Rev. B 40, 7574-7589 (1989).
[9] D. Allen, R. Shad, G. Zangari, I. Zana, D. Yang, M. Tondra and D Wang, "Pinhole imaging in magnetic tunnel junctions," J. Appl. Phys. 87, 5188-5190 (2000).
[10] C. A. Klein, "Bandgap dependence and related features of radiation ionization energies in semiconductors," J. Appl. Phys. 39, 2029-2038 (1968).
[11] W. L. Barnes, "Fluorescence near interfaces: The role of photonic mode density," J. Mod. Opt. 45, 661-699 (1998).

Appendix D : Two-Photon Absorption in CdSe Quantum Dots Embedded in Sol-Gel Films

Yanrui Zhao†, Li Wang, Weiliang Chen, R. K. Jain

Center for High Technology Materials, the University of New Mexico

1313 Goddard, SE Albuquerque, NM 81706
† Tel: (505) 272-7891 Fax: (505) 272-7801 E-mail: yrzhao@chtm.unm.edu

Abstract: Sol-gel films containing CdSe quantum dots are promising materials for nonlinear optical waveguide devices. We describe quantitative measurements of the two-photon absorption (TPA) coefficient at 820 nm in such films, as well as the spectral dependence of TPA-induced fluorescence over the 730-980 nm wavelength range.

OCIS codes: (190.0190) Nonlinear Optics

1. Introduction

Semiconductor quantum dots have emerged as important materials for several optoelectronic devices, notably lasers and amplifiers, and also appear to have significant potential for nonlinear optical waveguide devices, both for all-optical switching (via both Kerr and TPA effects) applications, and for optoelectronic demultiplexer-type switches. In this regard, sol-gel films embedded with quantum dots are particularly promising because of the relative simplicity of their fabrication, and the relatively widespread availability of CdSe quantum dots of varying dot diameters (in colloidal suspensions), commercially and otherwise, as relatively simple "starter" materials for waveguide devices based on such films. In this presentation, we describe quantitative measurements of the two-photon absorption (TPA) coefficient at 820 nm in such films, as well as the spectral dependence of TPA-induced fluorescence over the 730-980 nm wavelength range.

The phenomenon of TPA in bulk semiconductor materials is generally quite well understood [1-3]. Measured values of the TPA coefficients in bulk semiconductor materials are also in good agreement with theory. In low-dimensionality systems, such as nanocrystals, quantum size effects drastically change the electronic energy spectra, and significant enhancements are expected in the value of the TPA coefficients [4] at appropriate resonant wavelengths. Furthermore, studies of the TPA spectra are of significant interest, since they add

valuable complementary information to information obtained via simple linear absorption spectroscopy [5]. Moreover, low-dimensional QD structures are very promising for improving the sensitivity of photoconductive TPA-based photodetection devices [6-9].

2. Experiments and Discussion

CdSe/ZnS core-shell QDs (of dot diameters = 1.9 nm, and size variation of less than 5 %) were embedded in a commercial UV curable sol-gel resin and deposited in a film of thickness = 126 μm. The concentration of the core QDs (by weight) was approximately 3%. The peak wavelength of the photoluminescence spectrum was at 486 nm, with a full-width-half-maximum (FWHM) of 37 nm, and the peak of the linear absorption was at 462 nm.

3.1 Measurement of TPA Coefficients

The TPA coefficients were measured at 820 nm via inverse transmission measurements, using a mode-locked Ti:Sapphire laser (of 100 fs pulse duration) with a repetition rate of 76 MHz and an average power of 500 mW. A lens of 5 cm focal length was used to focus the laser beam onto the sol-gel film.

The measured inverse transmission curve is shown in Fig. 1. From a linear fit of the measured data, we estimate a linear absorption coefficient of α_0=1.78 cm^{-1} and a TPA coefficient β =8.78 cm/GW with a <5% fitting error. Under the same conditions, a ZnSe bulk crystal -- measured as a reference sample – yielded values of α_0 =2.45 cm^{-1} and β =3.97 cm/GW for the linear and TPA absorption coefficients. These measurements of the ZnSe reference material are reasonably close to published values of β (5.5 cm/GW at 532 nm, corresponding to 4.05 cm/GW at 820 nm) for ZnSe bulk crystals [3]. Considering the 3% core weight percentage of the quantum dot composition of our sol-gel films, the measured value of β of 8.78 cm/GW is quite high, indicating the potential of such quantum dots for enhanced sensitivity TPA devices (by increasing the QD density or weight %).

3.2 Fluorescence Measurements

TPA-induced fluorescence was measured while tuning the Ti:Sapphire laser between the wavelengths of 730 nm and 980 nm. A photomultiplier tube (PMT) was used to detect the integrated fluorescence signal. The fluorescence signal vs. incident intensity was measured at several pump wavelengths, and a quadratic relationship between the fluorescence signal and the incident power was verified, proving that the fluorescence was induced by TPA.

As seen in Fig. 2, the integrated fluorescence shows a peak at an excitation wavelength of ~800 nm. The insert shows the anticipated TPA coefficient in a CdSe-like bulk crystal whose bandgap is modified to 2.68 eV to correspond to that of the CdSe QDs used in our studies. The simulated TPA coefficient shows a peak at ~650nm and a FWHM of over 500 nm, differing significantly from the peak location of 800nm and FWHM of less than 100 nm observed in our studies. Although some of the peak shift and bandwidth reduction is partly attributable to reabsorption effects, we expect these contributions to be negligible; as such, these results clearly

point to significant differences in the TPA behaviour between quantum-confined structures and bulk crystals. In reality, a narrower excitation spectrum is expected from simple theoretical considerations. The observed width of 100 nm is not yet fully understood, and may be attributable to a broader size distribution than specified for our QDs. This issue is being currently investigated.

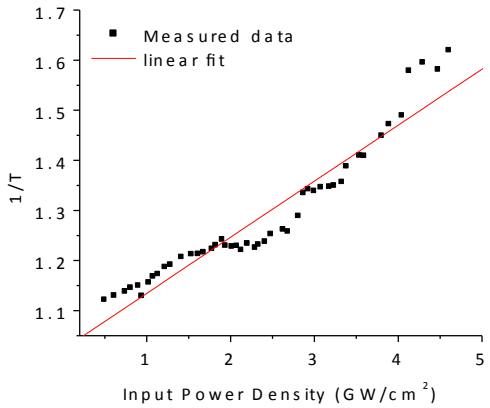

Fig.1: Inverse transmission measurement at 820 nm of a 126 micron thick sol-gel film containing CdSe quantum dots (3 % weight content) of 1.8 nm diameter.

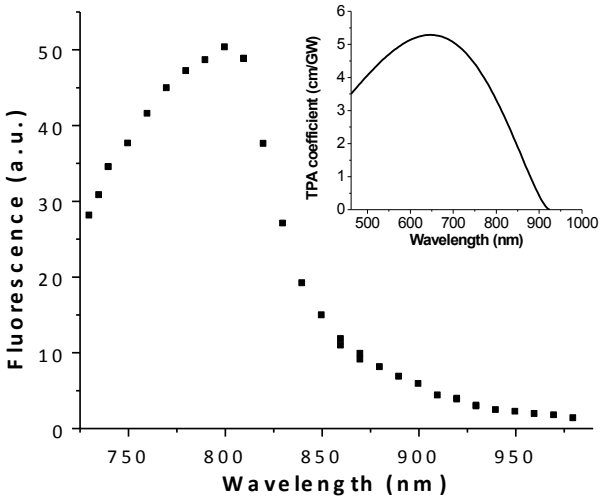

Fig. 2: TPA excitation spectrum of the CdSe QDs, obtained by plotting the integrated fluorescence as a function of the incident "pump" wavelength. The insert shows the anticipated spectral dependence of the TPA coefficient for a "CdSe-like" bulk crystal .

3. Conclusions

Measurements of the TPA coefficient and TPA-induced fluorescence of CdSe quantum dots in sol-gel films indicate the promise of these materials for future TPA devices, and show enhancements in the TPA coefficients and changes in spectral characteristics compared to their bulk counterparts.

Acknowledgements:

The authors thank AFOSR and the Department of Energy (DOE) for the support of this research and Prof. Malloy of the University of New Mexico for the loan of the Ti:sapphire laser used for these studies.

References:

[1] C. C. Lee and H. Y. Fan, " Two-Photon Absorption with Excitonic Effect for Degenerate Valence Bands", Phys. Rev B, 9, 3502 (1974)
[2] G. D. Mahan, "Theory of Two-Photon Spectroscopy in Solids", Phys. Rev., 170, 825 (1968)
[3] E. W. Van Stryland, M.A. Woodall, et. al, "Energy band-gap dependence of two-photon absorption", Optics Letters; 10, 490 (1985)

[4] A.V. Fedorov, A.V. Baranov, K. Inoue, "Two-photon transitions in systems with semiconductor quantum dots", Phs. Rev. B, 54, 8627 (1996)
[5] G. P. Banfi, V. Degiorgio, D. T. Fortusini, "Two-photon absorption coefficient measurements based on widely tunable femtosecond pulses from parametric generation, " Pure and Applied Optics; 7, 361 (1998)
[6] S. Schmittrink, D.A.B. Miller, D.S. Chemla, "Theory of the linear and nonlinear optical-properties of semiconductor microcrystals", Phys. Rev. B, 35, 8113 (1987)

[7] J. K. Ranka, A. L. Gaeta, A. Baltuska, M. S. Pshenichnikov and D. A. Wiersma, "Autocorrelation Measurement of 6-fs pulses Based on the Two-photon-incuded Photocurrent in a GaAsP Photodiode", *Optics Letters*, 22, 1344 (1997)

[8] H. K. Tsang, P. P. Vasilev, I. H. White, R. V. Penty and J. S. Aichison, "First Demonstration of Two Photon Absorption in a Semiconductor Waveguide Pumped by a Diode Laser", *Electronics Letters*, 29, 1660 (1993)

[9] K. Kikuchi, "Optical Sampling System at 1.5μm Using Two Photon Absorption in Si Avalanche Photodiode", *Electronics Letters*, 34, 1354 (1998)

Appendix E: Plasmonic Quantum Dots for Nonlinear Optical Applications

M. Klopfer, L. Wang and R. K. Jain

Center for High Technology Materials, University of New Mexico, 1313 Goddard St SE, Albuquerque, NM 87106

jain@chtm.unm.edu

Abstract: This presentation describes the design of novel plasmonic quantum dots for nonlinear applications, including labels for TPAF-based biomedical imaging, with projected fluorescence intensities >1000X higher than currently-used fluorescent labels.

OCIS codes: (170.6280) Spectroscopy, fluorescence and luminescence; (240.6680) Surface plasmons

1. Introduction

Two-photon absorption fluorescence (TPAF) has been demonstrated as a powerful tool for bio-imaging applications, particularly for deep-tissue imaging applications [1, 2]. TPAF is advantageous for biomedical applications due to the use of wavelengths in the tissue optical window of 600-1300nm. However the weak fluorescence signals from many fluorophores impose significant limitations to the maximum depths (usually around several hundred microns) that can be imaged with reasonable signal-to-noise ratios, for studies such as individual molecule labeling and tracking in intravital studies. Also they frequently contain the toxic element cadmium which limits their medical use.

During the last decade, semiconductor quantum dots (QDs) have attracted significant attention as fluorescent labels due to their significant advantages over other fluorophores: (a) broad absorption spectra and more readily tunable emission options (b) high quantum yields, (c) relatively high photochemical stability, and (d) relatively large two-photon absorption cross sections. Photodynamic therapy [4] is another biomedical application of TPAF where the photon generated by two photon upconversion is used to generate cytotoxic reactive oxygen species (ROS) in cancer tissue. Focusing the NIR light in the cancer tissue results in its selective destruction by the ROS. Targeting of the QDs to a desired tissue is acheived by functionalizing them with biomolecules causing increased accumulation in the target tissue which can improve their absorption for photodynamic therapy or enhance their brightness for imaging . We analyze the structure -- shown schematically in Fig. 1 -- consisting of a QD enclosed in a layer of silica enclosed in a thin shell of gold. This should eliminate the toxicity of the QD and as we show enhance the brightness of the QD. ***There has been a long-standing need for high-brightness, nonphotobleaching, and nontoxic fluorophores; a promising solution to this need -- such as that described here -- is expected to revolutionize the implementation of TPAF in numerous medical research and clinical applications.***

2. Related Work

Nevertheless, due to the stringent demands of numerous imaging applications, there have been numerous attempts to improve the brightness of QDs, including the use of surface-plasmon enhancement techniques [5] and the fabrication of complex SQD – gold nanoparticles assemblies for this purpose. Enderlein[5] used vector spherical harmonic (VSH) analysis for a SiO2/Ag core/shell structure and shows maximum enhancement on the order of 17 for a single shell thickness of 5 nm in a plot of wavelengths vs core radii. The range of core/shell sizes for maximum enhancement was not considered.

In this presentation we describe the design of novel plasmonic nanostructures in which the two-photon absorption-induced fluorescence signals are expected to be over 2 orders of magnitude higher than those from optimally-chosen CdSe SQDs, while mitigating the problems associated with toxicity of those SQDs.

3. Results

The proposed high-brightness light emitters consist of one or more QDs enclosed in an appropriate gold nanoshell, as shown schematically in Figure 1 (for the case of a single concentric QD structure), with an insulating layer between the QDs and the gold nanoshell to minimize nonradiative decay. To determine the field enhancement we used VSH for full EM analysis [6]. The model assumes nanoparticles that contain a CdSe core, a SiO2 layer, a gold layer and that the nanoparticle is surrounded by water/ aqueous tissue as is usual in bio-imaging applications. A 6nm QD was used in the model which has a fluorescent wavelength of 610nm. An excitation wavelength of 800 nm was chosen since it can be used for two photon excitation of the QD. Using VSH we show two novel behaviors of the electromagnetic field inside the nanoshell for use in TPAF. First we show that the maximum field enhancement

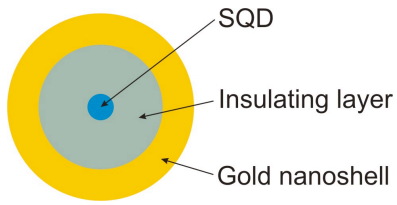

Fig. 1. Cross section of the SQD – gold nanoshell structure for high-brightness nanoparticles for imaging applications

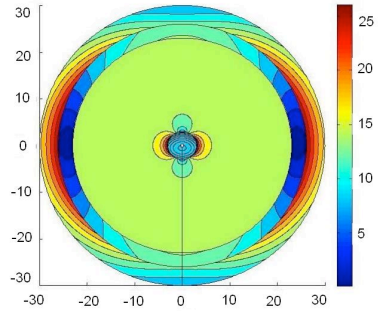

Fig. 2.Electric field enhancement for a 23nm silica core with 3nm gold shell and 800 nm wavelength

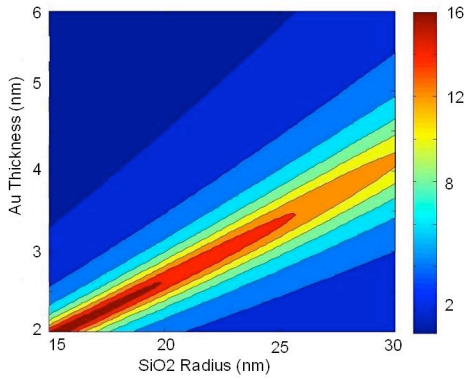

Fig. 3. Field enhancement at center of SiO2/Au core/shell nanoparticle.

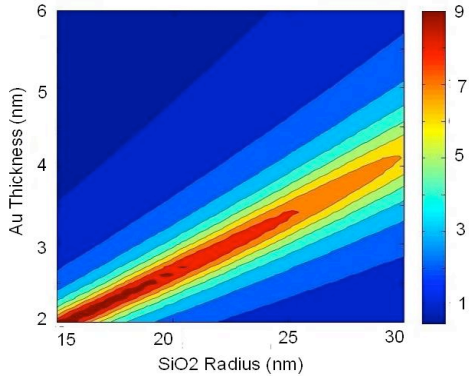

Fig. 4. Field enhancement at center of QD/SiO2/Au core/shell/shell nanoparticle.

structures and second that the field enhancement in a QD/SiO2/Au (QSA) core/shell/shell structure has decreased field enhancement in the QD compared to the field enhancement at the center of a SA nanoparticle. Furthermore we observe a large enhancement of the field around the QD which is even larger than the enhancement in the particle with no QD. This may be important for TPAF. Figure 3 shows the field enhancement at the center of an SA particle with various radii and thicknesses. The decreased maximum enhancement for larger core radii when using VSH doesn't appear when using the quasistatic model. Figure 4 shows the enhancement at the center of the QSA particle. It is clear that the enhancement is approximately half of the corresponding values for the SA particle. However as seen in the spatial plot of figure 2, the field enhancement close to the QD in the QSA structure reaches a value of 18 which is higher than the enhancement at the center of the SA particle of the same size.

The previous analysis is based on bulk values for the gold dielectric constant (-24.2, 1.46). In Fig. 5 we show the field enhancement for various core sizes using the dielectric constants at a wavelength of 800 nm for shell thicknesses shown in the legend.

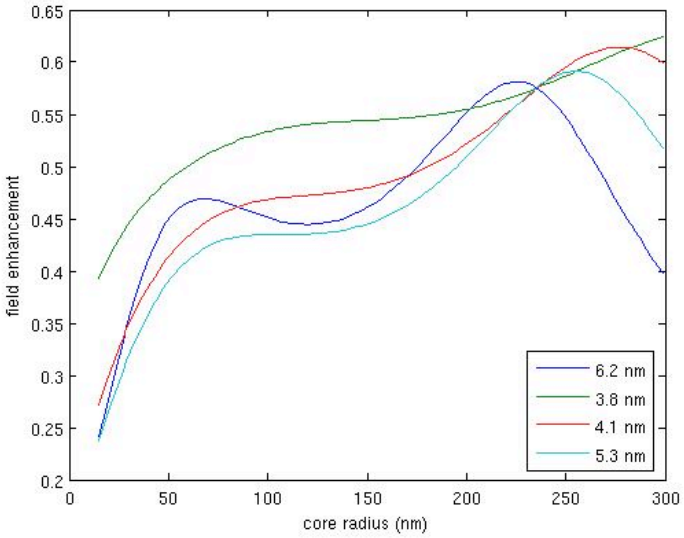

Fig. 5. field enhancement for shell thicknesses shown in legend

If the size dependent effect on the gold dielectric is close to the values obtained by [8] there will be very little field enhancement. However if the shells can be fabricated with a dielectric constant close to that of bulk gold then structures with an outer radius of 23 nm and shell thicknesses of 3 nm are expected to enable a TPAF signal enhancement of >2400 with fabrication tolerances that should be readily achievable by current chemical fabrication techniques [4]. Smaller core and thinner shell nanoparticle are expected to lead to larger TPAF signal enhancements but may be much more difficult to fabricate. We will discuss such issues in detail in our talk, along with the most exciting biological imaging applications foreseen for such ultrabright TPAF fluorophores in the foreseeable future.

4. References

[1] R. Larson, W. R. Zipfel, R. M. Williams, S. W. Clark, M. P. Bruchez, F. W. Wise, and W. W. Webb, "Water-soluble quantum dots for multiphoton fluorescence imaging in vivo," Science 300, 1434-1436 (2003).

[2] B. R. Masters, P. T. C. So, and E. Gratton, "Optical biopsy of in vivo human skin: Multi-photon excitation microscopy," Lasers in Medical Science 13, 196-203 (1998).

[3] A.E. Neeves and M. H. Birnboim, "Composite Structures for the Enhancement of Nonlinear-Optical Susceptibility," J. Opt. Soc. Am. B 6, 787-796 (1989).

[4] Yaghini, Elnaz, Alexander M Seifalian, and Alexander J MacRobert. 2009. Quantum dots and their potential biomedical applications in photosensitization for photodynamic therapy. *Nanomedicine* 4, no. 3 (4): 353-363.

[5] Enderlein, Jörg. "Spectral properties of a fluorescing molecule within a spherical metallic nanocavity," Physical Chemistry Chemical Physics 4, no. 12 (5): 2780-2786(2002).

[6] Le Ru, Eric, and Pablo Etchegoin. *Principles of Surface-Enhanced Raman Spectroscopy and related plasmonic effects.* 1st ed. Elsevier Science, December (2008).

Appendix F: Near-IR Emission from Metal-Insulator-Metal Tunnel Junctions Based on Surface Plasmon Interactions

J. Y. Chen, D. Ancukiewicz, L. Wang and R. K. Jain
Center for High Technology Materials, University of New Mexico, 1313 Goddard SE, Albuquerque NM 87106
jychen@chtm.unm.edu

jain@chtm.unm.edu

Abstract: We report the observation of near-IR emission from Al-AlO_x-Au tunnel junctions and a blurred-up peak at high applied voltage. We argue that it results from an interaction with near-IR surface plasmons.

OCIS codes: (130.0250) Optoelectronics; (130.3060) Infrared; (240.0310) Thin films

1. Introduction

An enhanced electron tunneling can be achieved through plasmon pumping in tunnel junctions (TJs) [1] and based on this light emission from TJs was achieved [2]. Since then both experimental and theoretical works have been done to explain this phenomenon [3-5]. It is generally agreed that the emission results from coupling between surface plasmon (SP) and photon at the metal-air interface through surface discontinuities.

In this paper, we report the observation of uniform light emission with spectrum extending from visible to near-IR region around 850nm from Al-AlO_x-Au tunnel junctions fabricated on gratings. Such near-IR emission cannot be observed from junctions fabricated on glass slide at low applied voltage, but will emerge when applied voltage is increased to 4.1V. Also it is noticed that the near-IR emission is usually accompanied by a spectrum shift towards longer wavelength. This uniform light emission may find application for broadband continuum light sources that require a large emission cone.

2. Experiments

Our tunnel junctions are deposited by thermal evaporation onto different sublayers including microscope glass slides, MgF_2 films and gratings. The MgF_2 film is directly deposited onto the glass slides with a thickness around 200nm. The grating has a period of 800nm and amplitude of 100nm. An Al film is deposited as the bottom electrode of the junction and the thickness is usually grater than 100nm. The Al layer is then thermally oxidized and covered with a 25-nm-thick Au film as the top electrode of the junction.

The junction has an area around $5mm^2$ and a resistance about 200Ω with DC applied voltage at 3.0V. The oxide layer thickness is around 3.5nm by a capacitance fitting. All the measurements are operated at room temperature.

3. Results

Fig. 1 shows the emissions from junctions fabricated directly on glass slides measured with increasing applied voltages from 3.9V to 4.1V. The spectra at 3.9V and 4.0V share a similar shape, but the spectrum obtained at 4.1V differs from the previous two with high emission intensity, blurred-up near-IR emission and a slight shift of visible emission peak. This near-IR emission is still observed when we reduce the applied voltage from 4.1V back to 3.9V, which indicates that some permanent changes have been made on the device structure. This is confirmed by studying the junction surface with an optical microscope, as shown in Fig. 3. The junction surface before measurements is much smoother than after the measurements. This roughened surface can explain the increased emission intensity that is related to the surface diffraction efficiency and then scales proportionally with the mean-square surface roughness [6]. Also the distribution of the surface roughnees has also been changed, which will result in a change in surface correlation length. We believe that the near-IR emission emerges as a result of this change.

Fig. 2 shows the emission from junctions fabricated on glass slide, MgF_2 film and periodic grating. While the first is measured at 4.0V, the latter two are measured at 3.5V and still exhibit much higher emission intensities. Again this should result from the difference in roughness scale. No near-IR emission is observed from junctions on MgF_2 because no approapriate surface discontinuity is available to make up for the wavevector difference between SP and light in that wavelength rang. This result agrees with the theoretical work of Laks and Mills [5]. The emssion spectrum from the junction on a grating has comparable visible emission intensity to that of junction on MgF2, and a much higher emission in near-IR region. There is little chance that this blurred-up 800nm peak is caused by decay of high-energy photons. It is more likely the result of near-IR surface plasmons being selectively coupled out with light by gratings based on the following equation (1), where a is the grating period, K_l is the free space light wavevector and K_{sp} is the surface plasmon wavevector excited by Al-AlO_x-Au junctions [7]. The calculation shows that the 800nm gratings make up for the wavevector difference between free space light and Au fast-mode surface plasmons.

$$K_l = K_{sp} - n \cdot \frac{2\pi}{a} \qquad (1)$$

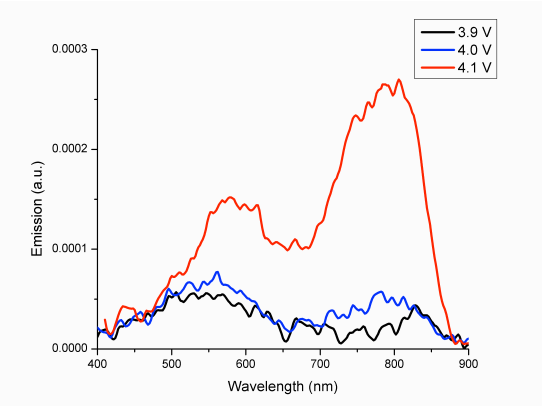

Fig. 1: Emission spectra from the tunnel junction fabricated on a glass slide with different DC applied voltages

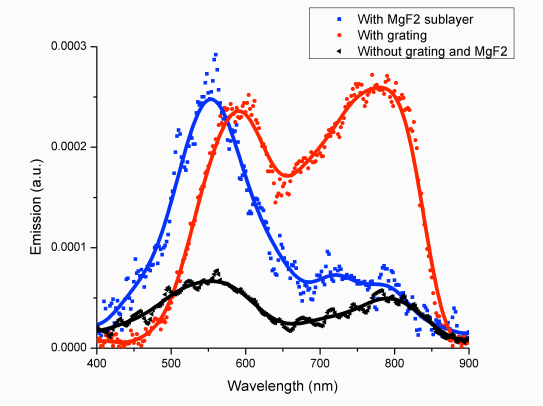

Fig.2: Emission spectra from tunnel junctions fabricated on glass slide, MgF_2 and grating respectively

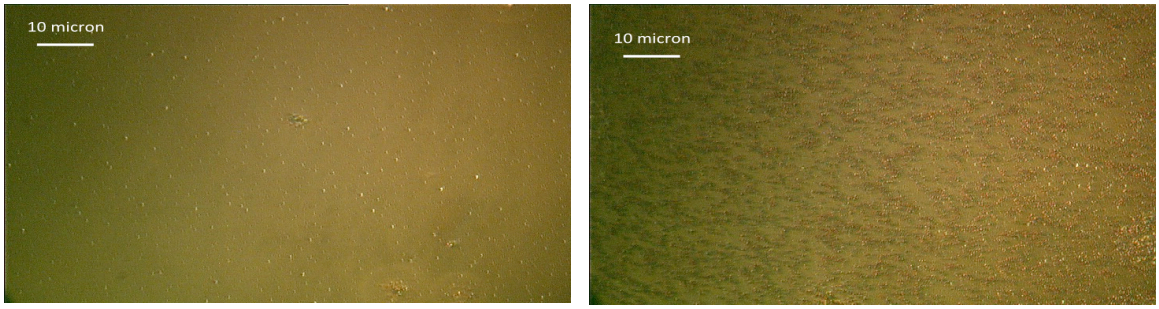

Fig. 3: Images of junction surface (a) before and (b) after spectral measurement

Note that there is usually a spectrum shift to lower energy when near-IR emission emerges. The mechnism is not yet totally understood, but this might be related to the increase of surface roughness [4]. Also the exact root mean square roughness and correlation length of the top metal surfaces are required for further quantitative analysis.

The device can work stably at 3.5V for one hour under room temperature, but breaks down much more easily when applied voltage is increased above 4V. This should be associated with the dielectric breakdown that occurs when electric field exceeds 10^9 V/m in aluminum oxide [8].

4. References

[12] D. P. Siu, R. K. Jain and T. K. Gustafson, "Stimulated electron tunneling in metal-barrier-metal structures due to surface plasmons," Appl. Phys. Lett. 28, 407-410 (1976)
[13] J. Lambe and S. L. McCarthy, "Light emission from inelastic electron tunneling," Phys. Rev. Lett. 37, 923-925 (1976).
[14] R. K. Jain, S. Wagner and D. H. Olson, "Stable room-temperature light emission from metal-insulator-metal junctions," Appl. Phys. Lett. 32, 62-64 (1977).
[15] J. Kirtley, T. N. Theis and J. C. Tsang, "Light emission from tunnel junctions on gratings," Phys. Rev. B 24, 5650-5663 (1981).
[16] B. Laks and D. L. Mills, "Photon emission from slightly roughened tunnel junctions," Phys. Rev. B 20, 4962-4980 (1979).
[17] B. Laks and D. L. Mills, "Roughness and the mean free path of surface polaritons in tunnel-junction structures," Phys. Rev. B 21, 5175-5184 (1979).
[18] P. D. Sparks and J. E. Rutledge, "Light emission from random rough tunnel junctions," Phys. Rev. B 40, 7574-7589 (1989).
[19] D. Allen, R. Shad, G. Zangari, I. Zana, D. Yang, M. Tondra and D Wang, "Pinhole imaging in magnetic tunnel junctions," J. Appl. Phys. 87, 5188-5190 (2000).